LIMNOLOGY and OCEANOGRAPHY

ASLO

Limnol. Oceanogr. 66, 2021, S363–S382

doi: 10.1002/lno.11676

Biogeochemical and ecological variability during the late summer–early autumn transition at an ice-floe drift station in the Central Arctic Ocean

Nicole L. Schanke,[1] Francesco Bolinesi,[2] Olga Mangoni,[2] Christian Katlein,[3] Philipp Anhaus,[3] Mario Hoppmann,[3] Peter A. Lee,[1] Giacomo R. DiTullio[1]*

[1]Hollings Marine Laboratory, College of Charleston, Charleston, South Carolina
[2]Dipartimento di Biologia, Università degli Studi di Napoli Federico II, Naples, Italy
[3]Helmholtz-Zentrum für Polar-und Meeresforschung, Bremerhaven, Germany

Abstract

As the annual expanse of Arctic summer ice-cover steadily decreases, concomitant biogeochemical and ecological changes in this region are likely to occur. Because the Central Arctic Ocean is often nutrient and light limited, it is essential to understand how environmental changes will affect productivity, phytoplankton species composition, and ensuing changes in biogeochemistry in the region. During the transition from late summer to early autumn, water column sampling of various biogeochemical parameters was conducted along an ice-floe drift station near the North Pole. Our results show that as the upper water column stratification weakened during the late summer–early autumn transition, nutrient concentrations, particulate dimethylsulfoniopropionate ($DMSP_p$) levels, photosynthetic efficiency, and biological productivity, as estimated by $\Delta O_2/Ar$ ratios, all decreased. Chemotaxonomic (CHEMTAX) analysis of phytoplankton pigments revealed a taxonomically diverse picoautotrophic community, with chlorophyll (Chl) c_3-containing flagellates and the prasinophyte, *Pyramimonas* spp., as the most abundant groups, comprising ~ 30% and 20% of the total Chl *a* (TChl *a*) biomass, respectively. In contrast to previous studies, the picoprasinophyte, *Micromonas* spp., represented only 5% to 10% of the TChl *a* biomass. Of the nine taxonomic groups identified, $DMSP_p$ was most closely associated with *Pyramimonas* spp., a Chl *b*-containing species not usually considered a high DMSP producer. As the extent and duration of open, ice-free waters in the Central Arctic Ocean progressively increases, we suggest that enhanced light transmission could potentially expand the ecological niche of *Pyramimonas* spp. in the region.

The Arctic Ocean comprises one of the most rapidly changing marine ecosystems in the world's oceans (Meredith et al. 2019). Over the last two decades, surface air temperatures in the Arctic have warmed at more than twice the global average (Meredith et al. 2019). Transport of warmer water masses from the Atlantic and Pacific Oceans has resulted in 2–4 times greater heat fluxes into the Arctic Ocean in the last four decades (Meredith et al. 2019). This increase in Arctic Ocean heat content has reduced sea ice extent, thickness, and growth. Atmosphere–ocean–sea ice changes have reduced the ice albedo of the Arctic Ocean and have caused a polar amplification response of 1.5–4.5 times the global mean warming (Holland and Bitz 2003). Recent models predict that nearly complete loss of Arctic sea ice cover in summer will likely occur during the first half of the 21st century, with the distinct possibility of total loss within a decade or two (Overland and Wang 2013). With a greater proportion of open water, the physical, chemical, and biological aspects of the Arctic Ocean are expected to change rapidly with significant alterations to ecosystem dynamics.

In late summer, as the Arctic Ocean sea ice reaches its annual minimum, a strong halocline from melting sea ice and relatively weak summer winds typically results in severe nutrient limitation in the surface waters (Codispoti et al. 2013). However, wind stress across an increasingly open Arctic Ocean could potentially erode the summer stratified upper layer, facilitating the turbulent diffusion of nutrients across the summer halocline (Tremblay and Gagnon 2009). At the same time, the projected decrease in areal sea ice expanse will

*Correspondence: ditullioj@cofc.edu

Additional Supporting Information may be found in the online version of this article.

Author Contribution Statement: All authors made significant contributions to the data presented in and/or the construction of this manuscript.

Special Issue: Biogeochemistry and Ecology across Arctic Aquatic Ecosystems in the Face of Change. Edited by: Peter J. Hernes, Suzanne E. Tank and Ronnie N. Glud

increase light penetration into the water column and allow for a longer growing season (Arrigo et al. 2008). Yet, as late summer progresses into early autumn, freeze-up conditions caused by colder air temperatures will alter the properties of the Arctic Ocean surface waters. Decreases in sea surface temperatures and increases in sea surface salinities, resulting from brine exclusion during ice formation, cause convective mixing of the upper water column. This instability in the upper water column may replenish macronutrients to nutrient-depleted surface waters. During the autumn freeze-up process, light transmittance into the water column diminishes rapidly, as snow accumulation and the freezing of melt ponds and open leads occurs. In an environment understood to be nutrient and light limited (Li et al. 2009; Tremblay and Gagnon 2009; Alou-Font et al. 2016), it is unclear how the predicted decrease in summer ice extent and the seasonal transition to refreezing conditions will affect primary production, phytoplankton community structure, and biogeochemical cycling.

Various estimates of net community production, from changes in nutrient inventories, dissolved inorganic carbon, and ΔO_2/Ar ratios, reveal significant biogeographical variability in different sectors of the Arctic Ocean (Codispoti et al. 2013; Ulfsbo et al. 2014). Significant primary production rates have been measured on Arctic continental shelves despite relatively low light and temperature conditions (Carmack and Wassmann 2006; Arrigo et al. 2008). However, current net community production estimates are relatively low for the Central Arctic Ocean due to both light and nutrient limitation on primary production (Popova et al. 2010; Codispoti et al. 2013; Ulfsbo et al. 2014). In the near future, unprecedented levels of open water in the late summer are expected to relieve light limitation effects, while possibly maintaining the Central Arctic Ocean as an oligotrophic system (Damm et al. 2010). Yet, as the areal expanse of summer sea ice continues to diminish, wind stress in early autumn could cause episodic turbulent diffusion of nutrients into the photic zone, potentially fueling late summer phytoplankton blooms (Codispoti et al. 2005; Ardyna et al. 2014; Lewis et al. 2019).

At present, there is a paucity of data regarding short-term variability in phytoplankton community structure in the Central Arctic Ocean, especially during the late summer. Rapidly changing environmental conditions have already altered the ecological balance in food web structure, resulting in a shift from sympagic microalgal species, such as sea ice diatoms, to a more planktonic picoeukaryotic-dominated community consisting of small chlorophyll (Chl) *b*-containing species (i.e., prasinophytes; Gradinger 1996; Lovejoy et al. 2007; Li et al. 2009, Blais et al. 2017). *Micromonas* spp., the most common Chl *b*-containing picoeukaryote in the Arctic, have been described as key sentinels of a warming Arctic Ocean (Worden et al. 2009; Demory et al. 2019). For example, *Micromonas* spp. have been shown to significantly increase growth rates at higher temperatures, even under low-light saturation intensities of $\sim 10\ \mu E\ m^{-2}\ s^{-1}$ (Lovejoy et al. 2007; Hoppe et al. 2018). Other prasinophyte species, such as *Pyramimonas* spp., have also been observed in the sea ice and water column of the open Arctic Ocean (Gradinger 1996; Harðardóttir et al. 2014). The continued progression of the Arctic Ocean phytoplankton community from sympagic species toward a more picoplankton-based food web will likely lead to a reduced carbon export flux due to enhanced microzooplankton grazing rates, compared to a microphytoplankton-dominated community (Sherr and Sherr 2002). This change in the Central Arctic Ocean food web structure will likely enhance the microbial loop and regenerated production, thereby significantly impacting various biogeochemical cycles in the region (Worden et al. 2015).

One of the major climatically important biogeochemical cycles involves the production of dimethylsulfoniopropionate (DMSP) and the release of volatile dimethylsulfide (DMS) to the atmosphere (Charlson et al. 1987). Particulate DMSP ($DMSP_p$), the precursor of DMS, is produced by some phytoplankton species and can serve as both a cryoprotectant and an osmolyte, protecting species living in a fluctuating environment influenced by ice formation and melt water (Stefels 2000; Lyon et al. 2016). The DMSP cleavage product, DMS, reacts to form sulfur aerosols and cloud condensation nuclei upon entering the atmosphere, potentially impacting the earth's radiation budget (Charlson et al. 1987).

Production of $DMSP_p$ varies among phytoplankton taxonomic groups (Keller et al. 1989). Many chromophytic (Chl *c*-containing) phytoplankton classes, such as dinoflagellates and prymnesiophytes, are significant producers of DMSP (Keller et al. 1989; Stefels 2000). However, sea ice diatoms may also significantly contribute to the DMSP pool, especially when found in high abundances (Levasseur et al. 1994; DiTullio et al. 1998). Prasinophytes and other Chl *b*-containing picoplankton do not typically produce large quantities of DMSP, yet intracellular DMSP concentrations may be greater than other groups due to their relatively small size (Keller et al. 1989). Although DMSP production rates of Arctic prasinophytes are unknown, a recent lab study of 16 Antarctic phytoplankton species observed similar DMSP production rates between *Pyramimonas gelidicola* and the high DMSP-producing haptophyte *Phaeocystis antarctica* (Sheehan and Petrou 2020). With a shift in the phytoplankton community from sea ice diatoms to picoeukaryotes, the future role of the Arctic Ocean as a significant source of these climatically relevant sulfur compounds remains unclear.

The major aim of this study was to characterize the evolution of phytoplankton production and community structure during the transition from late summer to early autumn. Our main hypothesis was that hydrographic changes in the upper water column during this seasonal transition would support a light and nutrient-limited picoeukaryotic phytoplankton community dominated by prasinophytes (i.e., *Micromonas* spp.) that would significantly impact biogeochemical cycling in the region.

Methods

The research presented here was performed within the framework of the U.S.–Sweden Joint Arctic Research Initiative.

This study was based on data collected during the Microbiology-Ocean-Cloud-Coupling in the High Arctic (MOCCHA) expedition aboard the Swedish Icebreaker *Oden* (RVIB *Oden*) to the Central Arctic Ocean in the late summer 2018. The overall objective of MOCCHA was to understand ocean-ice-atmosphere dynamics in the Central Arctic Ocean during the late summer transition period when refreezing begins. Several of the datasets discussed in the following sections have been made available online (see Supporting Information).

Sampling site

The RVIB *Oden* was anchored to an ice floe close to the geographic North Pole to set up a Lagrangian drift experiment from 19 August 2018 to 14 September 2018 (i.e., Julian days 231–257). The initial position of the ice floe was at 89.584°N, 39.192°E, and it remained close to this latitude until 01 September (day 244). During the following 2 weeks (days 244–257), the ice-floe drifted approximately 120 km southwards, reaching a position of 88.484°N, 38.174°E at the end of the planned drift (Fig. 1). In the following discussions on geographic positioning, the ice floe and the RVIB *Oden* will be considered as a single entity.

Hydrological and meteorological data

Meteorological data (including wind speed, direction, and air temperature) were collected from RVIB *Oden*'s foremast and were averaged over 30-min intervals. A Metek uSonic-3 heated sonic anemometer (Elmshorn, Germany) was used to measure wind speed and direction, and a Heitronics KT15.IIP infrared temperature sensor (Wiesbaden, Germany) reported air temperature measurements (Prytherch 2019).

After mooring to the ice floe, conductivity, temperature and depth (CTD) casts were conducted from aboard the RVIB *Oden* daily, as weather and sea ice conditions permitted. Hydrographic data (temperature, salinity, and density) and water samples were collected to depths of 200 or 1000 m using a Sea-Bird SBE 9 CTD (Bellevue, Washington) with a 24-bottle rosette. Data from the down-casts were processed using the Seasave software (version 7.26.7.107). Hydrographic data allowed for the quantification of water column stratification through determination of the mixed layer depth, defined here as the depth at which the density of the water column was 0.125 kg m^{-3} greater than the surface density for each CTD cast (Levitus 1982). Water column stability (E) and Brunt–Väisälä frequency (N^2) were calculated according to Knauss and Garfield (2017). These statistics provide additional information about the structure of the water column, with higher values of both E and N^2 representing steeper density gradients.

Light transmittance

Under-ice light transmittance was measured in a grid pattern under a 100 × 100 m survey area using a remotely operated vehicle (ROV; M500, Ocean Modules, Sweden) deployed away from the ship to prevent any shading effects. A hyperspectral radiometer (Ramses-ACC/VIS, TriOS, Germany) mounted on the ROV measured downwelling irradiance in a wavelength range of 320–950 nm. An identical sensor mounted on a tripod on the sea ice surface recorded synchronous incident irradiance. Sea ice light transmittance was calculated by dividing the reading of the under-ice sensor by the respective surface measurement. Details about the ROV system and data processing can be found in Nicolaus and Katlein (2013) and Katlein et al. (2017).

Nutrients

Seawater samples were syringe-filtered using sterile 0.22-μm Millipore filters and kept frozen until analysis. Macronutrient concentrations (nitrate, nitrite, phosphate, silicate, and ammonium) were measured at Stockholm University using

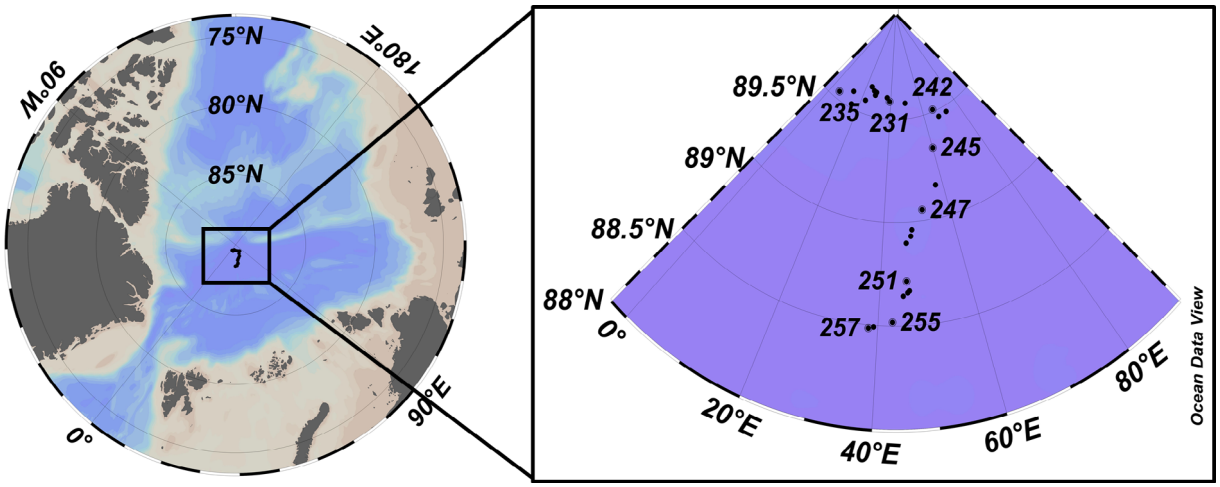

Fig 1. Map of RVIB *Oden* locations from 19 August (Julian day 231) to 14 September (Julian day 257), 2018. Dots represent ship location, with selected locations labeled with Julian day (1 = January 1) for reference.

standard colorimetric techniques on an autoanalyzer (detection limits: nitrate = 0.05 μmol L^{-1}, nitrite = 0.02 μmol L^{-1}, phosphate = 0.02 μmol L^{-1}, silicate = 0.05 μmol L^{-1}, ammonium = 0.2 μmol L^{-1}). The ratios of nitrate to phosphate were calculated and are reported as N : P values. The fraction of inorganic nitrogen available as regenerated nitrogen (F_{reg}) was calculated as $F_{reg} = \frac{[NH_4^+]}{[NO_3^-]+[NO_2^-]+[NH_4^+]}$ (Eppley and Peterson 1979). Our estimate of regenerated nitrogen, however, represents a lower bound to total regenerated nitrogen as urea concentrations were not measured.

Phytoplankton pigments

Two liters of seawater were collected from each depth by CTD and were filtered onto GF/F (Whatman) filters and stored at −80°C until samples were processed upon return from the expedition (approximately 2 months later). For analysis, pigments were extracted overnight in 1390 μL of high-performance liquid chromatography (HPLC)-grade acetone and 10 μL trans-β-Apo-8′-carotenal (internal standard) at −20°C. Approximately 24 h later, 600 μL of extract were 0.2 μm syringe-filtered and run on an Agilent 1100 Series HPLC, equipped with diode array and fluorescence detectors (Agilent Technologies, Santa Clara, California). This HPLC method utilized a Waters Symmetry C8 column (4.6 × 150 mm, 3.5 μm packing size), with binary mobile phases of methanol : acetonitrile : 0.25 mol L^{-1} pyridine (50 : 25 : 25 v : v : v) and methanol : acetonitrile : acetone (20 : 60 : 20 v : v : v; DiTullio and Geesey 2002). Pigment concentrations were calculated from resulting chromatograms using Agilent's ChemStation software (version B.03.02). Pigment standards were either isolated from pure phytoplankton cultures or obtained from DHI Lab Products (Hørsholm, Denmark). Detection limits were approximately 1 ng and the coefficient of variance for replicate injections was approximately 2%.

Relative abundance of several major algal groups was calculated from pigment concentrations using the matrix factorization program CHEMTAX (version 1.95; Mackey et al. 1996). Eleven pigment markers were used to define nine algal groups, according to the Lee et al. (2019) study conducted in the Chukchi and East Siberian Seas and the Coupel et al. (2015) study in the Beaufort Sea (Table S3). Initial pigment ratios used in the CHEMTAX analysis were based on the low light (subsurface Chl maximum) ratio matrix used in Lee et al. (2019). However, the initial pigment ratios for the diatom group were altered from Lee et al. (2019) to reflect the ratios of Chl $c_1 + c_2$ and fucoxanthin that were found in the overlying sea ice diatom community during our expedition (W. Smith unpubl.). The remaining eight algal groups include: (1) dinoflagellates (dinoflagellate-1 class, containing peridinin), (2) Chl c_3-flagellates (i.e., dinoflagellate-2 class lacking peridinin, raphidophytes, and silica-containing dictyochophytes), (3) cryptophytes (containing alloxanthin), (4) chrysophytes-pelagophytes (containing 19′-butanoyloxyfucoxanthin), (5) prymnesiophytes (haptophyte-7 class, containing 19′-hexanoyloxyfucoxanthin, like *Chrysochromulina* spp.), (6) *Pyramimonas* spp. (prasinophyte-2 class, lacking prasinoxanthin), (7) *Micromonas* spp. (prasinophyte-3 class, containing prasinoxanthin), and (8) chlorophytes (containing lutein and Chl *b*) (Coupel et al. 2015). Samples were analyzed using a series of independent depth bins to account for changes in pigment ratios resulting from photoacclimation (DiTullio et al. 2003). The depth bins used were: 0–5, 5–10, 10–20, 20–30, 30–40 m, with the same initial ratio matrix being used for each bin. Averages were taken of the results from any sample being grouped into two depth bins to increase sample number.

A turbulence profiler (MSS90L, Sea & Sun Technology, Trappenkamp, Germany) was regularly used from an access hole in the ice to obtain 192 profiles of seawater properties between 19 August and 14 September 2018. The profiler was operated in free-falling mode to a depth of up to 600 m and retrieved using an electrical winch. Measured parameters were mainly temperature, salinity, pressure, velocity shear, and Chl *a* fluorescence, recorded at a frequency of 512 Hz. In this study, only the Chl *a* fluorescence data (in relative fluorescence units) were used for further processing and calibration. The profiler fluorometer was a Turner Designs CYCLOPS-7 Submersible Fluorometer (San Jose, California) with an excitation wavelength of 465 nm, a minimum detection limit of 0.03 μg L^{-1}, and a linear range between 0 and 500 μg L^{-1}. The high-resolution raw fluorescence data were linearly interpolated to a depth grid of 0.1 m and calibrated using in situ total Chl *a* concentrations derived from HPLC analyses.

Photosynthetic efficiency

Photosynthetic efficiency was measured using a Phyto PAM phytoplankton analyzer (Walz, Effeltrich, Germany). Pulse–amplitude–modulation measurements are based on the selective amplification of a fluorescence signal detected after an intense and short pulse of saturating light (>3000 μmol photons m^{-2} s^{-1} for 0.8 ms) released by light-emitting diodes. By using the quantitative relationship between Chl *a* fluorescence and the efficiency of photosynthetic energy conversion, values of the photosynthetic efficiency of photosystem II can be calculated from the fluorescence yield before (Fo) and after (Fm) the saturation pulse. Photosynthetic efficiency of photosystem II is reported as Fv/Fm, where Fv = (Fm − Fo) (Genty et al. 1989). Photosynthetic efficiency values provide insight on the photochemical competency of photosystem II and its ability to convert light energy into fixed carbon.

All samples were acclimated in the dark for 30 min at 0°C before analysis of photosynthetic efficiency so that all reactions centers were in the open state and nonphotochemical dissipation of excitation energy was minimal. Measurements were blank-corrected before analysis by filtering seawater through a 0.2-μm filter (Cullen and Davis 2003). In order to estimate the fraction of absorbed quanta used for photosystem

II photochemistry, photosynthetic efficiency of photosystem II as Fv/Fm was measured for each sample following the method reported in Maxwell and Johnson (2000).

Size-fractionated Chl *a*

In order to evaluate phytoplankton size classes, size-fractionated Chl *a* samples were collected by passing 1 L of seawater through a serial filtration system using 2- and 20-μm filters (Nuclepore). Filtrate from the 2-μm filters was collected onto GF/F (Whatman) filters. These filters were stored at −20°C until analyzed with a Shimadzu spectrofluorometer (Kyoto, Japan) according to the protocol described by Holm-Hansen (1965). Size classes were defined as microphytoplankton (>20 μm), nanophytoplankton (2–20 μm) or picophytoplankton (<2 μm). Data are reported as the size classes' percent contribution to total Chl *a* (TChl *a*).

Dissolved gases

Instrumental determination of O_2, Ar, DMS, and methane was carried out using membrane inlet mass spectrometry. The system consists of a Pfeiffer Vacuum quadrupole mass spectrometer equipped with a HiCube 80 pumping station, a QMA 200 analyzer, and a flow-through silicone capillary membrane inlet (Bay Instruments, Easton, Maryland) for sample introduction. The inlet is a glass vacuum line incorporating a U-tube and support for the 0.51-mm ID Silastic tubing membrane and 0.5-mm ID stainless steel capillary supply lines. The sample was pumped through the inlet system at 1.5 mL min^{-1} using a Gilson Minipuls 3 peristaltic pump (Middleton, Wisconsin). Before entering the membrane, the sample passed through a 75-cm length of capillary tubing immersed in a thermostated water bath (VWR, Suwanee, Georgia) and held at 20°C to ensure constant temperature and membrane permeability as the gasses passed through the membrane.

The U-tube section of the vacuum line (located between the membrane inlet and mass spectrometer) was immersed in either liquid nitrogen (for methane analyses) or an isopropanol bath held at <−45°C (for DMS analyses) to remove water vapor from the gas stream before introduction of the stream into the mass spectrometer. In this configuration, the system maintained an average (± standard deviation) operating vacuum pressure of $3.0 \pm 0.4 \times 10^{-7}$ mbar during methane analyses and $2.0 \pm 0.2 \times 10^{-6}$ mbar during DMS analyses. The sample liquid was pumped from the bottom of the sample bottle and through the membrane until the mass spectrometer signal stabilized (typically a minimum of 6 min). Using the secondary electron multiplier detector, DMS was monitored by scanning at m/z 62 for 20 s, CH_4 at m/z 15 for 20 s, O_2 at m/z 32 for 0.1 s, and Ar at m/z 40 for 0.5 s.

Calibration for DMS was carried out with freshly prepared DMS standards made from seawater collected at 1000 m and commercially available DMS. The detection limit for DMS was 0.05 nmol L^{-1}. Calibration for methane was carried out using 1000 m seawater bubbled with 99% methane. The methane standards were equilibrated at 8°C and 20°C, and the methane concentrations were calculated using Bunsen Coefficients taken from Yamamoto et al. (1976). The detection limit for methane was 5 nmol L^{-1}.

ΔO_2/Ar ratios

Percentages for ΔO_2 and ΔAr, along with ΔO_2/Ar ratios were calculated as qualitative indicators of biological activity following the formula of Nicholson et al. (2010):

$$\Delta X = \left(\left[\frac{(X)_{\text{sample}}}{(X)_{\text{sat}}} \right] - 1 \right) \times 100,$$

where $(X)_{\text{sample}}$ is the ion current for each mass (or ratio of O_2 to Ar) measured in the seawater sample and $(X)_{\text{sat}}$ is the corresponding measurement for an air-equilibrated saturation standard. A new saturation standard was generated for each sequence of samples (DMS or methane) run on the mass spectrometer by sparging a separate surface sample collected at the same time as the main samples with ambient air for a minimum of 20 min (c.f. Tortell et al. 2011, 2012). These standards were generated at least once per day when samples were being collected.

Measurements of DMSP

Collection and preservation of water samples for dissolved and total DMSP ($DMSP_d$ and $DMSP_t$, respectively) analysis was carried out following the small-volume gravity-filtration and microwave preservation protocols of Kiene and Slezak (2006) and Kinsey and Kieber (2016). A 7 mL aliquot of sample was collected for $DMSP_t$. A second aliquot of sample was gravity filtered through a GF/F filter and the first 7 mL of filtrate were collected for the $DMSP_d$ sample. The samples were heated in a 1000-W microwave for 7 s and acidified with 70 μL of 50% sulfuric acid (Ricci Chemical, Arlington, Texas). Sample preparation was carried out at room temperature. Once prepared, all DMSP samples were stored at 4°C until analysis. The samples were base hydrolyzed in strong alkali (sodium hydroxide; final concentration, 2 mol L^{-1}) and analyzed for DMS as per Barak-Gavish et al. (2018). Calibration of the membrane inlet mass spectrometer was carried out with freshly prepared DMSP standards made using enriched artificial seawater (35 g L^{-1}; Harrison et al. 1980) and commercially available DMSP powder (Research Plus, Bayonne, New Jersy). The detection limit for the system was 0.1 nmol L^{-1}. Particulate DMSP was calculated postanalysis as $DMSP_t$ less $DMSP_d$.

Statistical analysis

In order to investigate the relationships between several of the biological and environmental variables, a principal component analysis based on a Spearman's correlation matrix was utilized. Missing data were removed with pairwise deletion and a significance level of $\alpha = 0.05$ was used to determine the presence of a correlation between variables. The number of observations for each variable included in the analysis varied

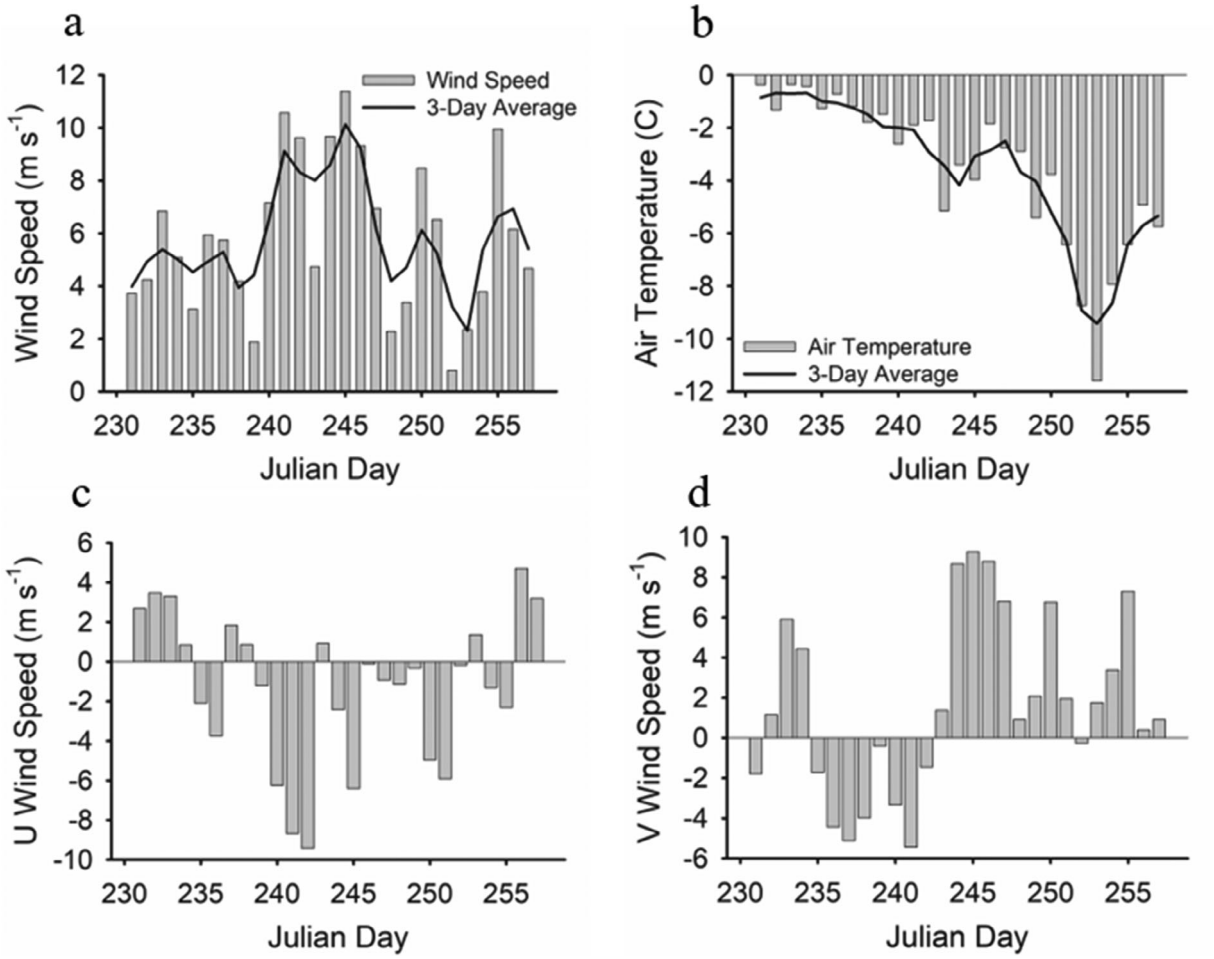

Fig 2. (**a**,**c**,**d**) Wind speed and (**b**) air temperature measurements from day 231 to day 257. (**c**) U-wind speed is that in the east–west direction, with positive values coming from the east and negative values coming from the west. (**d**) V-wind speed is that in the north–south direction, with positive values coming from the north and negative values coming from the south. Bars represent daily averages. Lines plotted in (**a**) and (**b**) are 3-day averages, as calculated by the average from the day before, day of and day after reported date.

from 118 (total Chl *a*) to 53 (Fv/Fm). The principal component analysis and Spearman's correlation matrix were run using XLSTAT-Ecology 2019 software. Results from Spearman's correlation matrix are discussed among the following results, while outputs from the principal component analysis are included in Supporting Information.

Results

During the 4-week sampling period, the geographical location of the ice floe to which the RVIB *Oden* was anchored changed as a result of meteorological forcing (Fig. 1). From the initial position on 19 August (day 231), the ice-floe drifted zonally along 89.5°N until 01 September (day 244), covering a total of 109 km, with approximately 62 km between the furthest sampling locations. After 01 September, the ice floe began to drift southwest. Over the following 13 d, the ice floe moved a total of 133 km, the majority of which occurred while ice and weather conditions prohibited CTD casts (days 243–250). Sample collection did not resume until 08 September (day 251), after the ice floe had drifted 94 km from the previous sampling location (day 242).

Meteorology

During the sampling period, a wind event occurred during which wind speed increased and wind direction shifted (Fig. 2a,c,d). From days 240 to 247, the 3-day wind speed averages were greater than 6 m s^{-1}, with a maximum wind speed of 11 m s^{-1} on day 245. At the beginning of this event (days 240–242), winds were from the southwest, however, by day 244 the strongest winds were from the north (Fig. 2c,d). Wind speeds before day 240 and after day 247 were lower, with 3-day average speeds of 2–7 m s^{-1}. The days during which the strongest winds from the north occurred were also the days during which the location of the ice floe began to move south.

Air temperature slowly decreased from day 231 (−1°C) to day 241 (−2°C) (Fig. 2b). Days 243–245 exhibited temperatures down to −4°C, but the coldest air temperatures occurred from day 249 throughout the duration of the sampling period (day 257), with 3-day average temperatures of −4°C to −9°C and a minimum of −11.6°C on day 253. These weather conditions led to refreezing of melt ponds in the area surrounding the ice floe.

Hydrography

CTD casts were conducted daily as long as the access hole at the stern of the RVIB *Oden* could be kept free of ice. During the northerly wind event, the ice floe moved to the southwest, presumably due to Ekman drift. Wind stress, ice drag, and brine exclusion during refreezing contributed to a deepening of the mixed layer depth during days 251–257, compared to days 231–242 (Fig. 3). Temperature and salinity plots indicate that the meridional advection was likely not associated with any significant changes in subsurface water masses between 200 and 1000 m (Fig. S1a).

During days 231–242, hydrographic conditions were relatively stable in the upper 100 m of the water column (Fig. 3). The average (± standard deviation) mixed layer depth was 17 ± 1 m (Table 1) and was characterized by temperatures ranging from −1.6°C to −1.7°C and salinities between 31.5 and 32. However, freezing of the surface waters and shoaling of warmer, saltier water from below altered the water column in the upper 100 m during days 251–257. Here, the mixed layer depth increased to 25 ± 3 m (Figs. 3, S1b–d; Table 1). The surface mixed layer (upper 30 m) was influenced by a freezing event from days 251 to 255, as evidenced by an increase in salinity, which also occurred during the 5 days of the coldest air temperatures (Fig. 2b). During this period, surface water temperatures were below −1.8°C and salinities ranged from 32 to 32.5. A steep isopycnal (density = 1026 kg m^{-3}) was observed from days 251 to 257 (Fig. 3c), indicative of the sinking of saltier surface waters due to brine exclusion during ice formation.

Water column stability (E) and Brunt–Väisälä frequency (N^2) were calculated at the mixed layer depth for each CTD cast (Table 1). These statistics provide insight into the structure of the water column, with higher E and N^2 values representing steeper density gradients and lower values representing a greater degree of mixing. Both E and N^2 were greater during days 231–242, indicating more highly stratified surface waters, than during days 251–257 (with the exception of day 255). The lower E and N^2 values on days 251–257 are representative of a less stratified, more well-mixed water column. However, the surface waters on day 255 were more highly stratified, as local maxima of E and N^2 were present (Table 1).

The changes in the upper 100 m of the water column from days 231–242 to 251–257 are consistent with the transition from late summer to early autumn. The warmer, fresher, more stratified water column present during days 231–242 is characteristic of the environmental conditions of the late summer, while the deepening of the mixed layer depth driven by colder, saltier water, resulting from refreezing conditions during days 251–257 is representative of the early autumn environment. For consistency in reporting the following results, data describing the surface mixed layer will include those from the upper 20 m during the late summer (days 231–242) and the upper 30 m during the early autumn (days 251–257), based on the mixed layer depths during those days. Vertical profiles of

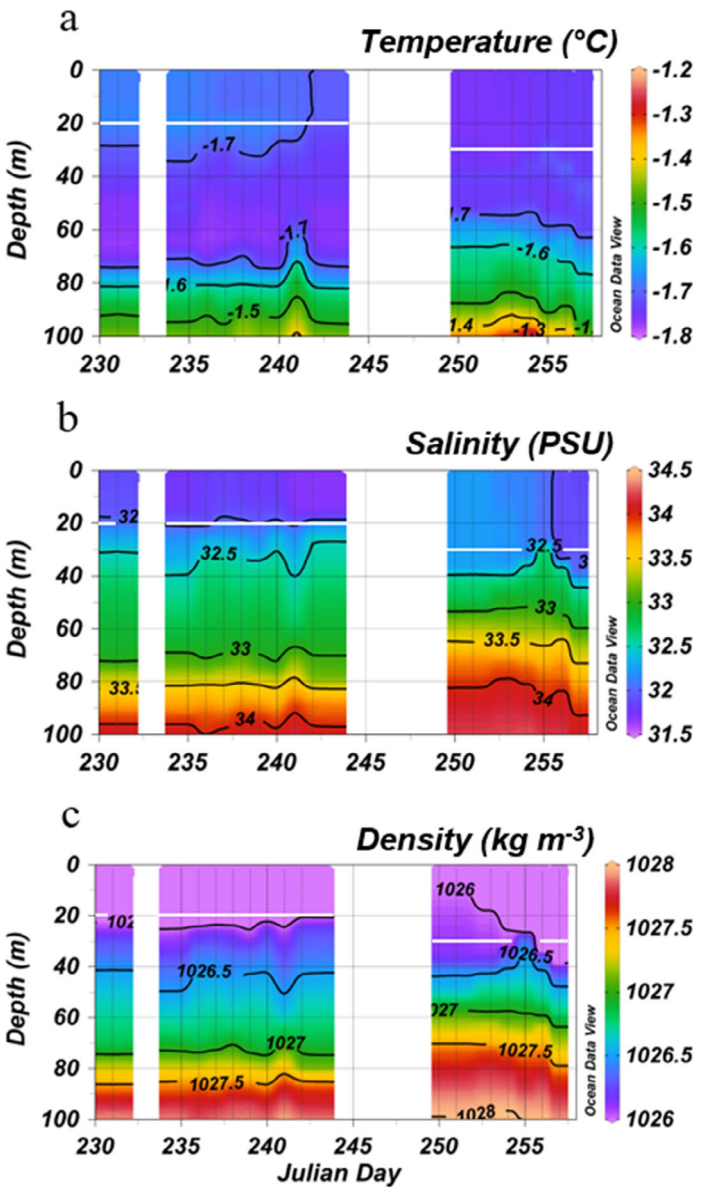

Fig 3. (**a**) Temperature, (**b**) salinity, and (**c**) density data collected by CTD from days 231 to 257. White horizontal lines represent the mixed layer depth at 20 m during the late summer (days 231–242) and at 30 m during the late autumn (days 251–257).

Table 1. Coordinates and mixed layer depth (MLD) of the CTD cast from each day. The MLD was determined to be the depth at which the density of the water column was 0.125 kg m^{-3} greater than the surface density of each CTD cast. Water column stability (E) and Brunt–Väisälä frequency (N^2) are reported for the MLD.

Julian day	Latitude (°N)	Longitude (°E)	MLD (m)	E ($\times 10^{-8}$ m^{-1})	N^2 ($\times 10^{-4}$ s^{-1})
231	89.5843	39.1915	17	950	0.93
235	89.5357	5.1870	17	6237	6.12
236	89.5179	15.3715	19	3794	3.72
237	89.5643	22.6512	17	7918	7.77
238	89.6219	26.7642	15	984	0.97
239	89.6373	24.1212	17	2222	2.18
240	89.6033	28.3372	15	2607	2.56
241	89.5756	49.9514	18	3662	3.59
242	89.5101	66.1233	17	3052	2.99
251	88.7158	45.9789	27	525	0.52
253	88.6604	46.1363	19	573	0.56
254	88.6444	45.1291	26	554	0.54
255	88.5177	42.8607	26	1619	1.59
256	88.4923	39.1941	29	481	0.47
257	88.4843	38.1741	24	748	0.73

temperature, salinity, and density demonstrate the change in mixed layer depths that occurred between the late summer and early autumn (Fig. S1b–d).

Light transmittance

Frequency distributions of under-ice light transmittance within a representative 100×100 m grid on the ice floe showed a decrease in transmittance throughout the sampling period (Fig. 4). Level ice thickness was highly variable, but was typically 1–2 m thick, with many melt ponds and open leads visible during the beginning of the sampling period. On day 231, less than 20% of the surface incident irradiance passed through the sea ice, with average transmittance values around 5% to 10% (Fig. 4a). Eleven days later (day 242), the average light transmittance decreased to approximately 3%, with maximum transmittance near 10% of the surface incident irradiance (Fig. 4b). Light transmittance through the sea ice was less than 5% on days 251 and 256, with average values near 3% of the surface incident irradiance (Fig. 4c,d). This decrease in light transmittance is consistent with observed freeze-up conditions of the early autumn, as air temperatures decreased, snow accumulation increased, and melt ponds and open leads in the surrounding area began to close (Fig. 2b).

Nutrients

Overall, the surface mixed layer (< 20 m during late summer and < 30 m during early autumn) displayed relatively oligotrophic characteristics throughout the sampling period. Nitrate concentrations above the mixed layer depth averaged 1.3 ± 0.6 μmol L^{-1} in late summer and 1.2 ± 0.4 μmol L^{-1} in early autumn (Fig. 5a), but increased with depth, such that nitrate concentrations reached 11 ± 0.9 μmol L^{-1} near the nutricline at 100 m. The distribution of nitrate in the surface mixed layer varied minimally in the late summer. However, after day 251, the nitrate-depleted (<2 μmol L^{-1}) surface waters extended down to 40 m and nitrate-enriched (>5 μmol L^{-1}) deeper waters extended up toward 50 m, consistent with the deepening of the mixed layer and the shoaling of deep waters during the early autumn period.

The distribution of phosphate in the water column differed between late summer and early autumn, with respect to the mixed layer depth (Fig. 5b). During the late summer, phosphate was uniformly distributed above and below the mixed layer depth, with phosphate concentrations of 0.54 ± 0.09 and 0.7 ± 0.1 μmol L^{-1}, respectively. During the early autumn, phosphate in the surface mixed layer was relatively more depleted, with concentrations of 0.39 ± 0.05 μmol L^{-1}, while concentrations below the surface mixed layer were 54% higher (i.e., 0.6 ± 0.1 μmol L^{-1}). Throughout the entire sampling period, the highest phosphate concentrations occurred at 100 m (0.8 ± 0.1 μmol L^{-1}).

The average N : P ratio was well below the Redfield ratio for most of the samples collected (with the exception of those at 100 m on days 251, 254, and 256; Fig. 5e). Samples collected from the surface mixed layer in late summer had N : P values of 2.4 ± 0.9. Similar values were recorded above the mixed layer depth in the early autumn, with N : P ratios of 3.0 ± 0.8. Overall, N : P followed an almost identical trend as the concentration of nitrate (Fig. 5a), as N : P ratios increased with depth, reaching 14 ± 2 at the nutricline (100 m) across the entire sampling period.

Silicate concentrations in the surface waters were similar throughout the entire sampling period, with concentrations in the surface mixed layer of 4.5 ± 0.7 μmol L^{-1} in late

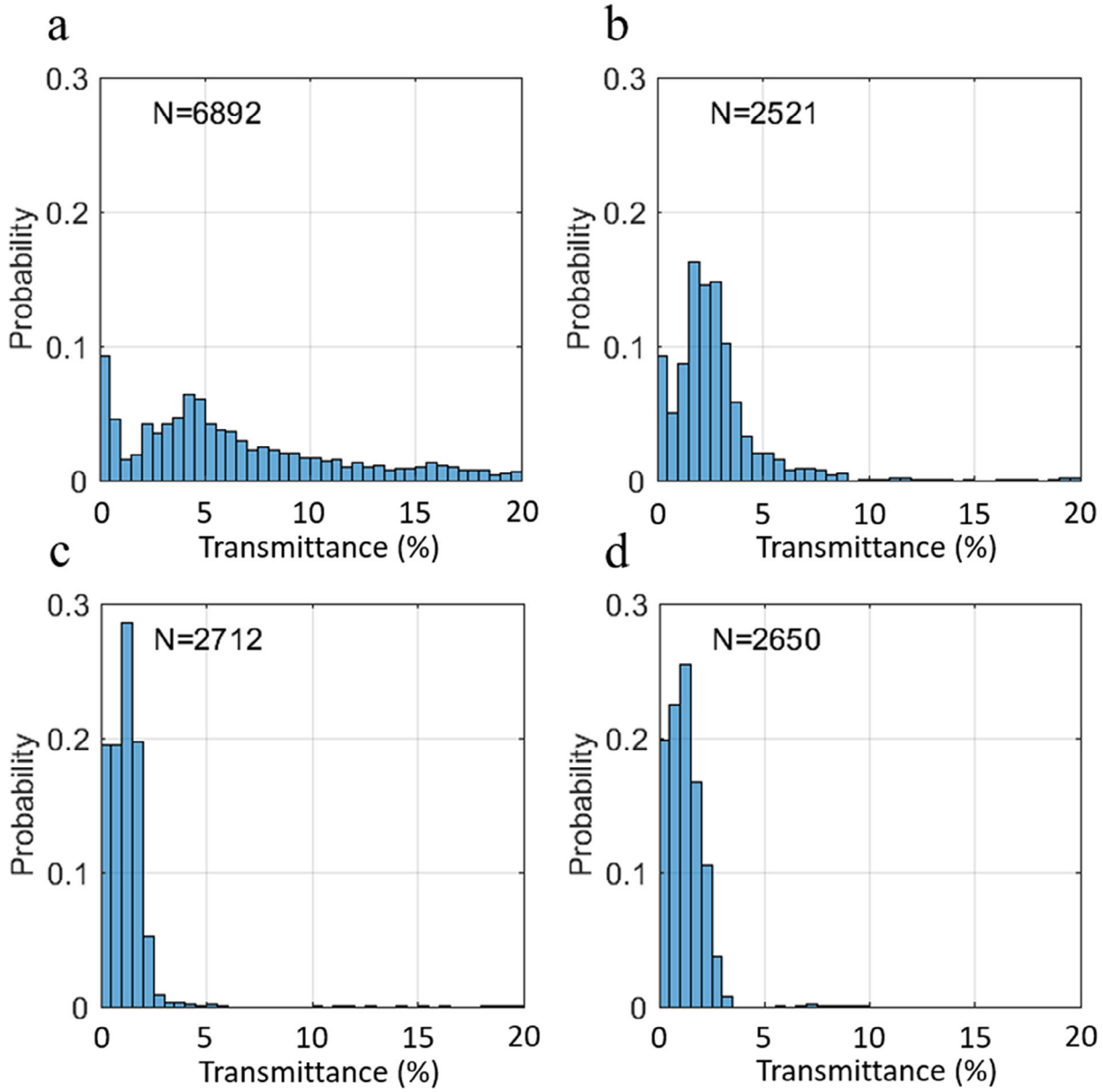

Fig 4. Frequency distributions of under-ice light transmittance from days (**a**) 231 and (**b**) 242 of the late summer and days (**c**) 251 and (**d**) 256 of the early autumn. *N* is the number of data points collected.

summer and 3.6 ± 0.4 μmol L^{-1} in early autumn. The lowest concentrations of silicate (3.1 ± 0.3 μmol L^{-1}) were found in the upper 20 m on days 251–252 (Fig. 5c). In a similar trend as nitrate and phosphate, silicate concentrations increased with depth toward the nutricline at approximately 100 m. During the late summer, the highest silicate concentrations were found at 75 m (7.7 ± 0.9 μmol L^{-1}), whereas during the early autumn, elevated silicate concentrations (6.5 ± 0.3 μmol L^{-1}) were observed shallower, at 50–75 m, as shoaling of deeper waters occurred.

The concentration of ammonium showed more temporal and spatial variability than the other macronutrients (Fig. 5d). During most of the late summer sampling, the highest ammonium concentrations were isolated in the surface mixed layer (0.9 ± 0.5 μmol L^{-1}), while concentrations below 20 m decreased to 0.3 ± 0.4 μmol L^{-1}. For the remainder of the sampling period (days 231 and 251–257), ammonium concentrations showed a higher but more uniform distribution with depth, as concentrations near 1 μmol L^{-1} (0.9 ± 0.4 μmol L^{-1}) were present throughout the upper 100 m. During both the late summer and early autumn, phaeopigments (pheophytin *a* and pheophytin *a*) were observed in the upper 40–60 m, with the highest concentrations being measured in the upper 20 m (Fig. S4b,c), where

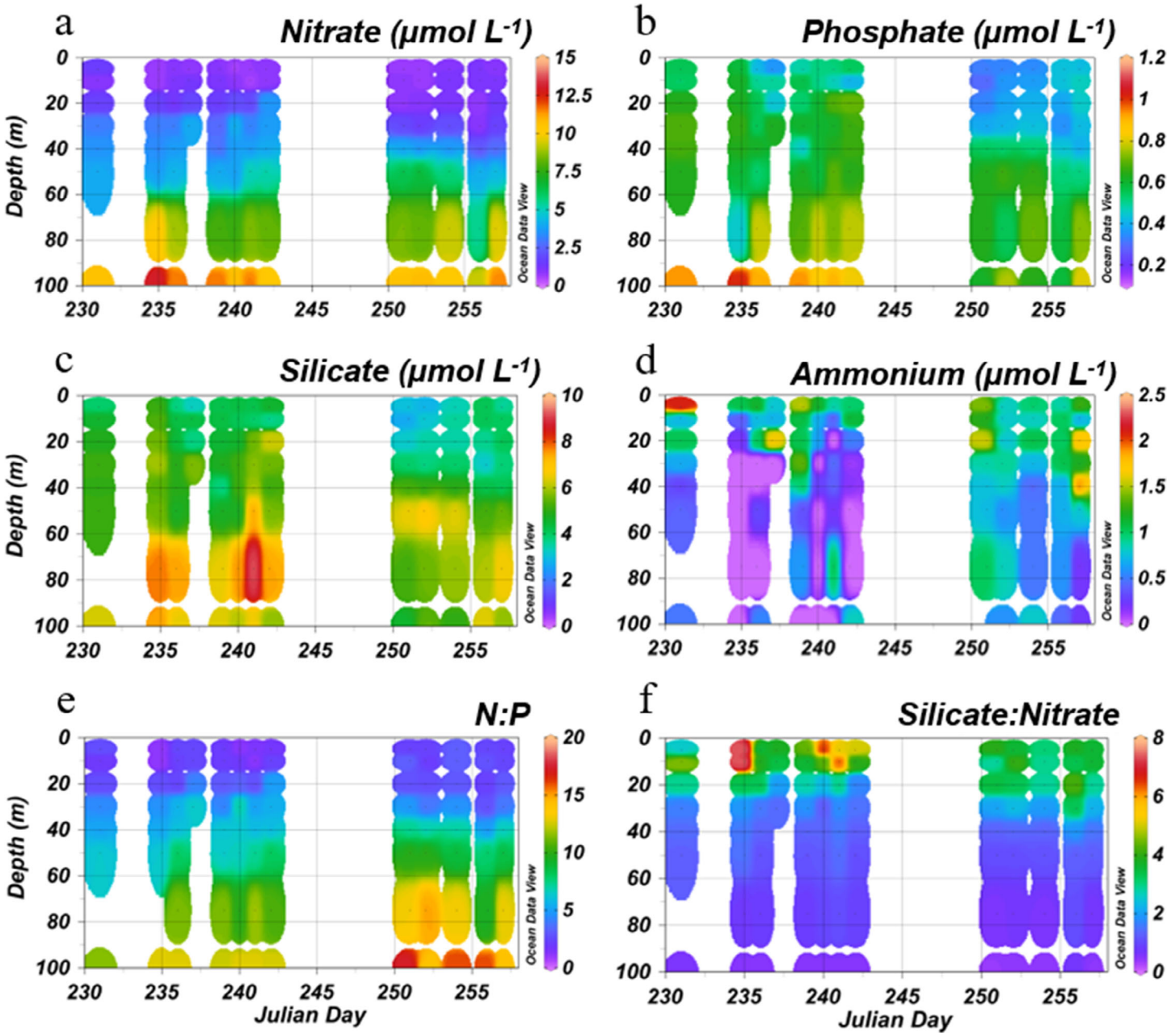

Fig 5. (**a**) Nitrate, (**b**) phosphate, (**c**) silicate, and (**d**) ammonium concentrations in μmol L^{-1}, and (**e**) nitrate : phosphate (N : P), and (**f**) silicate : nitrate ratios. Data are reported from days 231 to 257.

the highest concentrations of ammonium were also observed. These phaeopigments are indicative of zooplankton grazing processes. The presence of copepods in near surface waters was visually observed by ROV dives (Fig. S5a) and likely was responsible for the elevated ammonium levels as a byproduct of phytoplankton consumption.

The fraction of total inorganic nitrogen present as regenerated nitrogen (F_{reg}) serves as a statistic to better understand the source of nitrogen available to the microbial community. During the late summer, the highest F_{reg} values were found in the upper 10 m, averaging around 0.5 (0.48 ± 0.09) (Fig. S4a). Very similar F_{reg} values (0.48 ± 0.08) were present in the upper 20 m during the early autumn period. Below these depths, F_{reg} decreased to 0.1 ± 0.1 during the late summer and 0.2 ± 0.1 during the early autumn. With near surface F_{reg} values around 0.5, approximately 50% of the available inorganic nitrogen in the photic zone was present as ammonium.

Phytoplankton abundance and community structure

Phytoplankton biomass is reported here as TChl *a*, which includes Chl *a* + chlorophyllide *a*. Throughout the entire sampling period, most of the phytoplankton biomass was located above the mixed layer depth. Maximum TChl *a* concentrations reached approximately 350–400 ng L^{-1} in the upper 10 m on days 231 and 240–242, with minimal TChl *a* biomass observed below 40 m (15 ± 6 ng L^{-1}; Fig. 6a). During the late summer, TChl *a* concentrations in the surface mixed layer were 280 ± 80 ng L^{-1} and decreased to 200 ± 60 ng L^{-1} in the early autumn. During the early autumn period, the highest TChl *a* concentrations occurred on day 251 (303 ± 7 ng L^{-1}) and continued to decline over the final few days, with TChl *a* concentrations of 180 ± 20 ng L^{-1} in the surface mixed layer on days 256 and 257 (Fig. 6a).

Relative Chl *a* fluorescence readings from the turbulence profiler fluorometer were highly correlated with CTD TChl *a* profiles (linear regression: $r^2 = 0.85$, $p < 0.05$), providing high-resolution estimates of biomass, especially during days 243–250 when CTD sampling was not possible due to ice conditions (Fig. 6b). By including the estimated biomass during this transition period (days 243–250), the deepening of the mixed layer depth was observed as relatively high Chl *a*-estimated biomass (>100 ng L^{-1}) was measured at increasingly greater depths. Local maxima and minima in the estimated biomass data occurred on comparable days with the TChl *a* from the CTD profiles, as relatively high biomass was found in the surface mixed layer on days 231–232 and 236–240 and lower biomass was found on the final three sampling days (255–257; Fig. 6a,b).

Concentrations of TChl *a* and Chl *b* were integrated within the surface mixed layer on each sampling day (Table 2). Although there were not significant differences in TChl *a* and Chl *b* between the late summer and early autumn, there was a shift toward a greater abundance of Chl *b*-containing phytoplankton during the final three sampling days (days 255–257). While the Chl *b* : TChl *a* ratios during the late summer and most of the early autumn (days 251–254) were 0.26 ± 0.05 and 0.25 ± 0.01, respectively, this ratio increased by 26% to 0.34 ± 0.04 during days 255–257 (Table 2). Additional pigment data can be found in Figs. S2, S3.

The CHEMTAX program was used to define nine algal groups that contributed to the Central Arctic Ocean phytoplankton community. Because of relatively low TChl *a* biomass below the mixed layer depth, only the results of the CHEMTAX analysis from the upper 20 m (late summer) and 30 m (early autumn) are reported here. Averages of values from each depth bin (as defined in the methods) were taken to describe the community composition of the surface waters above the mixed layer depth. The phytoplankton community was relatively diverse, as all nine taxonomic groups were present on every sampling day, and only six samples contained a dominant group (i.e., >50% of the community; Figs. 7, S6)

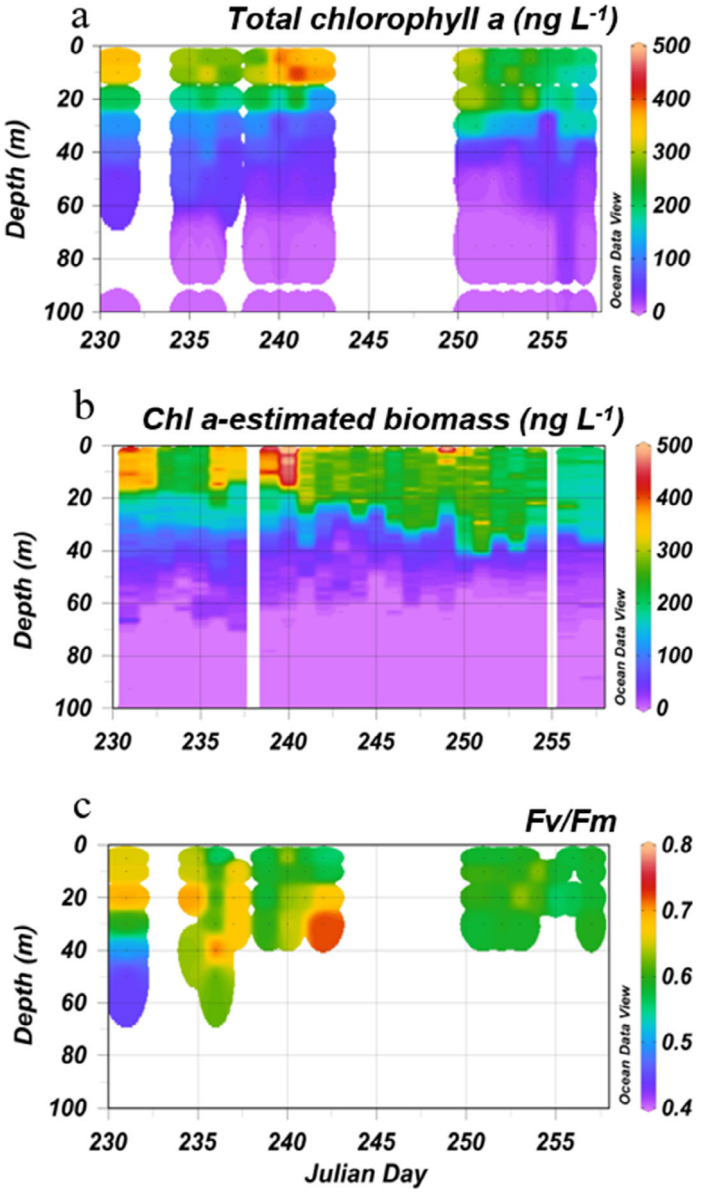

Fig 6. (**a**) Total chlorophyll *a* (Chl *a* + chlorophyllide *a*) concentration (ng L^{-1}), (**b**) Chl *a*-estimated biomass (ng L^{-1}) from calibrated high-resolution fluorescence data collected via turbulence profiler, and (**c**) photosynthetic efficiency of photosystem II as Fv/Fm from days 231 to 257.

Initial pigment ratios used and the final output ratios calculated by the CHEMTAX analysis are listed in Tables S3, S4, respectively.

Chl c_3 flagellates and *Pyramimonas* spp. were the most abundant taxa, accounting for water column averages of 34% ± 8% and 22% ± 5% of the TChl *a* biomass, respectively (Fig. 7). Chl c_3 flagellates were more prevalent with depth, especially on days 235–236 and 251–254, while *Pyramimonas* spp., a Chl-*b* containing picoeukaryote, was more abundant in the upper 10 m than deeper in the water column (Fig. S6). Dinoflagellates and chrysophytes-pelagophytes were the least

Table 2. Integrated total Chl *a* (TChl *a*) and Chl *b* concentrations, Chl *b* : TChl *a* and prasinoxanthin : Chl *b* (Prasino : Chl *b*) ratios and multiple regression analysis (MRA)-predicted integrated Chl *a* (Fujiwara et al. 2014) in the upper 20 m during the late summer (days 231–242) and in the upper 30 m during the early autumn (days 251–257).

Julian day	TChl *a* (mg m^{-2})	Chl *b* (mg m^{-2})	Chl *b* : TChl *a*	Prasino : Chl *b*	MRA Chl *a*
231	6.314	1.876	0.297	0.025	3.490
235	5.326	1.485	0.279	0.039	4.175
236	5.592	1.981	0.354	0.040	4.417
237	5.034	1.296	0.257	0.038	4.117
239	5.431	1.114	0.205	0.054	4.172
240	6.533	1.410	0.216	0.052	4.711
241	7.056	1.552	0.220	0.046	4.282
242	6.067	1.512	0.249	0.047	3.561
251	8.515	1.984	0.233	0.042	7.288
252	6.433	1.619	0.252	0.054	7.169
253	6.474	1.695	0.262	0.054	7.029
254	7.092	1.746	0.246	0.070	4.262
255	5.040	1.499	0.297	0.071	6.103
256	5.711	2.044	0.358	0.075	4.061
257	5.053	1.834	0.363	0.077	6.636

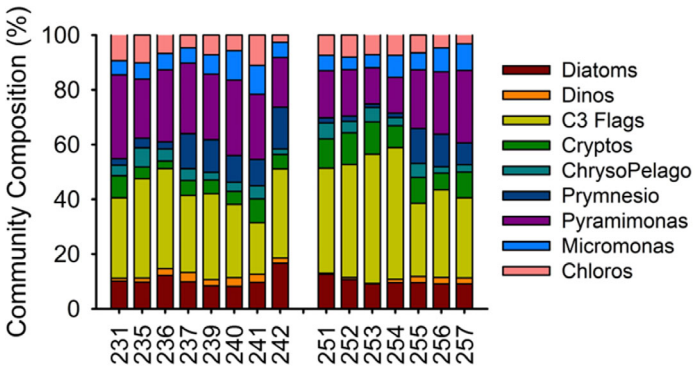

Fig 7. CHEMTAX results of phytoplankton community composition as percent contribution to total Chl *a* by nine algal groups: diatoms, dinoflagellates (Dinos), Chl c_3-containing flagellates (C3 flags), cryptophytes (Cryptos), chrysophytes-pelogophytes (ChrysoPelago), prymnesiophytes (Prymnesio), *Pyramimonas* spp., *Micromonas* spp., and chlorophytes (Chloros) from days 231 to 257. Data reported are average values from the upper 20 m during the late summer (days 231–242) and the upper 30 m during the early autumn (days 251–257), according to the respective mixed layer depths. No data were collected during days 243–250 due to sea ice conditions in the area.

abundant groups, with each representing less than 5% of the community. The remaining five taxonomic groups (diatoms, cryptophytes, prymnesiophytes, chlorophytes, and *Micromonas* spp.) contributed approximately 7% to 10% of the TChl *a* biomass (Fig. 7).

Diatom populations were presumably seeded from the melting sea ice, as visual observations from the ROV noted extensive blooms of bottom ice diatom communities including *Melosira* spp. (Fig. S5b). The diatom community consistently contributed about 10% (10% ± 2%) of the TChl *a* biomass throughout the surface waters (Fig. 7). The greatest diatom abundance was observed on day 242, the final sampling day of the late summer period, making up about 17% of the phytoplankton community (Fig. 7). The population of cryptophytes increased with depth from 5% ± 3% at 5 m to 13% ± 6% at 30 m (Fig. S6a,d), with an average abundance of 7% ± 3% of the phytoplankton community (Fig. 7). Cryptophytes were also measured in greater abundance during the early autumn (10% ± 2%) than the late summer (6% ± 2%). Prymnesiophytes (e.g., *Chrysochromulina* spp.) made up a small part (<10%) of the total phytoplankton community on days 231, 235, and 251–254. On the remaining days, prymnesiophytes showed a general trend of being more prevalent with depth (Fig. S6).

Chlorophytes were most often found at 5 m and became less frequent with depth (present on all 15 d at 5 m, 13 d at 20 m, and 6 d at 30 m), yet making up approximately the same small proportion of the community at each depth (7% ± 3% at 5 m, 8% ± 3% at 20 m and 7% ± 2% at 30 m; Fig. S6). *Micromonas* spp. contributed only 6% ± 2% of the TChl *a* biomass in the upper 10 m during most of the sampling period. However, on the final two sampling days (256–257), this value increased to 10% ± 2%, while a greater abundance of *Pyramimonas* spp., especially below 10 m, was also observed (Fig. S6). The increased prevalence of these Chl *b*-containing picoeukaryotes was also supported by higher Chl *b* : TChl *a* ratios on days 255–257 (Table 2).

Photosynthetic efficiency

Photosynthetic efficiency of photosystem II (as Fv/Fm) contributes to the description of the physiological state of the

phytoplankton and the efficiency with which it is able to convert light energy to fixed carbon via photosynthesis. Values for Fv/Fm were measured in the upper 40–50 m of the water column on most sampling days (Fig. 6c). These values ranged from 0.442 to 0.723 with an average of 0.61 ± 0.05 throughout the entire sampling period. During the late summer, average Fv/Fm values were higher and more variable (0.63 ± 0.04) than during the early autumn (0.59 ± 0.02). On days 231 and 235, photosynthetic efficiency decreased with depth. On days 240–242, the highest Fv/Fm values observed were from samples collected at 30 m while samples collected from 5 to 10 m revealed lower photosynthetic efficiencies. During the early autumn, when light transmittance had decreased (Fig. 4), Fv/Fm values were lower and displayed much less variation with day or depth than samples from the late summer (Fig. 6c).

Size-fractionated Chl *a*

Samples for size-fractioned Chl *a* were collected on days 231 and 251, the initial sampling days during the late summer and early autumn periods, respectively. Except for the community in the surface waters (5 m) on day 231, over 60% of the phytoplankton community in the surface mixed layer consisted of picophytoplankton (<2 μm) species (Fig. 8). Nanophytoplankton (2–20 μm) made up 66% of the TChl *a* at 5 m on day 231 but only 15% to 30% deeper in the water column. Larger (>20 μm) microphytoplankton species were the least abundant size class, contributing just $10\% \pm 6\%$ to the TChl *a*.

Methane, DMS, and DMSP

Both methane and DMS concentrations in the water column were consistently below our limit of detection. In the case of methane, our relatively high detection limit may have contributed to the lack of observable levels. Studies by Damm et al. (2010, 2015) have reported methane concentrations of 0–6 nmol L^{-1} in the Central Arctic Ocean with most of their measurements falling below 5 nmol L^{-1}. As such, the presence of methane at these levels would have been undetectable on our system during the expedition.

Modest levels of both $DMSP_d$ (0–5.8 nmol L^{-1}) and $DMSP_p$ (0–35.7 nmol L^{-1}) were observed during the expedition. Both DMSP pools showed considerable spatial and temporal variability, yet the highest levels were typically found in the surface mixed layer and declined rapidly to less than the limit of detection below 40 m (Fig. 9). Average concentrations of $DMSP_d$ and $DMSP_p$ in the surface mixed layer were greater and more variable during the late summer (1 ± 2 and 15 ± 11 nmol L^{-1}, respectively) than the early autumn (1 ± 1 and 9 ± 5 nmol L^{-1}, respectively). During the final two sampling days (days 256–257), $DMSP_p$ concentrations were slightly higher (11 ± 2 nmol L^{-1}) than the previous days of the early autumn period (Fig. 9b).

ΔO_2/Ar ratios

The ΔO_2/Ar ratios showed considerable variability during the sampling period (Fig. 10). Values ranged from 13.7 to −13.4 with higher values (typically equilibrium levels or supersaturation) being observed in the surface mixed layer while lower values (equilibrium levels or undersaturation) were observed below the mixed layer depth. This variability was not limited to samples collected from the CTD. Similarly, strong variations in oxygen saturation states were also observed in samples collected in the near-surface waters of a nearby open lead (14.1 to −1.8) and in under-ice water column samples collected with a Niskin bottle lowered through a hole in the ice (13.3 to −11.8). Additional discussion of the dissolved gas dynamics from these sampling sites will be presented elsewhere (Czerski, Lee et al. in prep.).

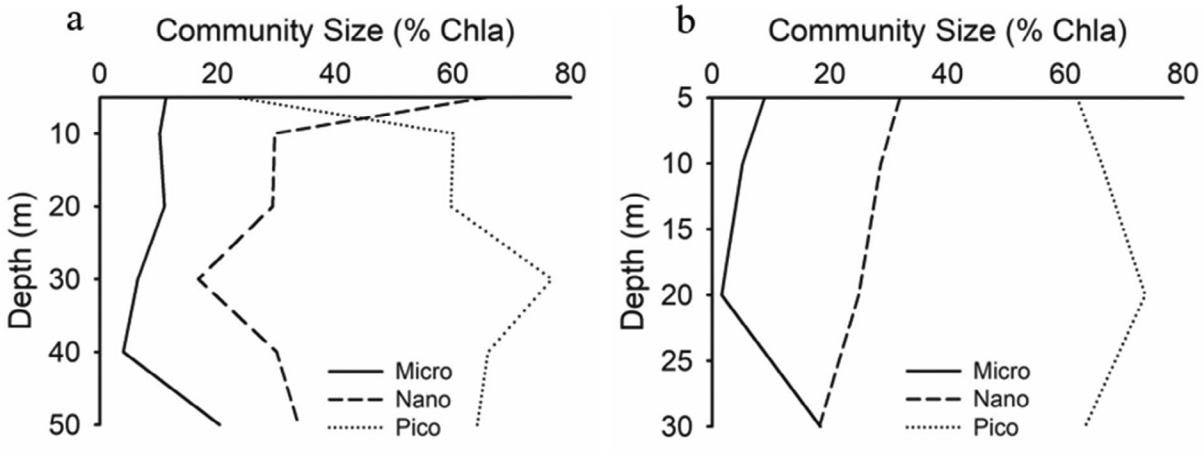

Fig 8. Proportion of Chl *a* contributed by phytoplankton size class as depth profiles on (**a**) day 231 during the late summer and (**b**) day 251 during the early autumn. Size classes are reported as microphytoplankton (>20 μm), nanophytoplankton (2–20 μm) and picophytoplankton (<2 μm).

Discussion

Our central hypothesis was that reduced irradiance and severe nutrient limitation in the photic zone would shift the microplanktonic phytoplankton assemblage to a more picoeukaryotic community dominated by Chl *b*-containing prasinophytes (such as *Micromonas* spp.) as late summer transitioned into early autumn. This seasonal change in the phytoplankton community could significantly affect various biogeochemical parameters such as reducing O_2/Ar ratios and DMS/DMSP concentrations, which are generally lower in Chl *b*-containing phytoplankton species (Keller et al. 1989). While prasinophytes were indeed observed as one of the dominant groups in the upper water column throughout the study period, pigment and CHEMTAX analyses revealed that *Pyramimonas* spp. and not *Micromonas* spp. were the primary species present within this taxonomic group (Fig. 7).

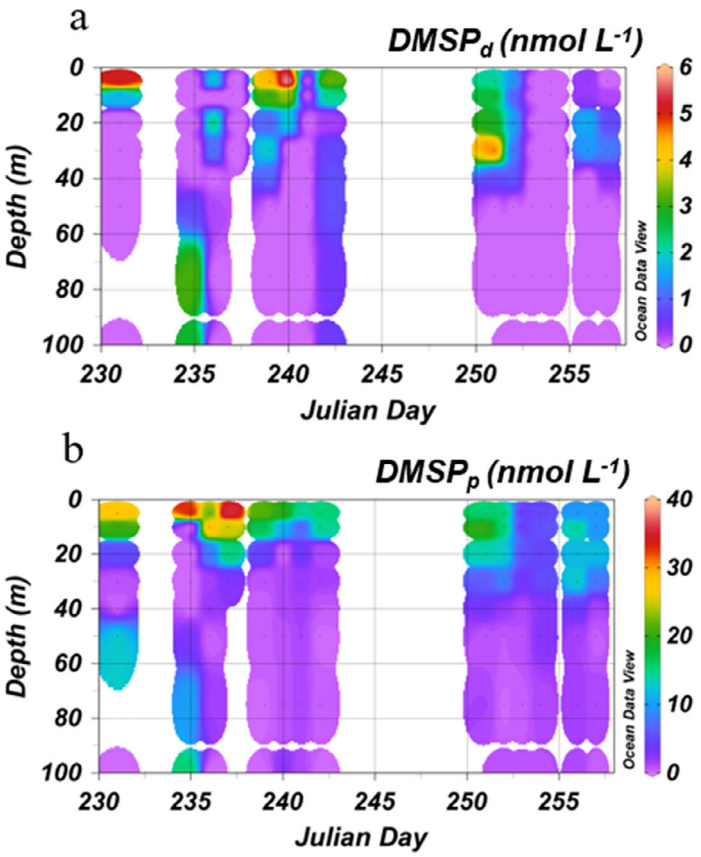

Fig 9. (**a**) Dissolved DMSP (DMSP$_d$) and (**b**) particulate DMSP (DMSP$_p$) concentrations in nmol L^{-1} from days 231 to 257.

Water column dynamics

During the transition from late summer (days 231–242) to early autumn (days 251–257), the upper 100 m of the water column displayed distinct biogeochemical differences, as the refreezing of melt ponds and open leads began. The water column during days 231–242 was characteristic of late summer-like conditions, with higher surface temperatures and lower surface salinities due to the presence of melt water. This resulted in a relatively more stable water column with a shallower mixed layer depth (approximately 20 m; Table 1) than observed at the end of the sampling period. Days 251–257 showed a distinct transition into early autumn as cold air temperatures during days 249–257 (Fig. 2b) caused freeze-up conditions. Ice formation and brine exclusion were noted by an increase in surface salinities between days 251 and 255 (Fig. 3b). The breakdown in water column stratification was evidenced by the transition from the warmer, fresher waters of the late summer to the colder, saltier waters of the early autumn, which likely resulted in enhanced convective mixing, extending the surface mixed layer toward 30 m (Fig. 3; Table 1). This increase in the mixed layer depth was likely due to double diffusion of heat and salt as the

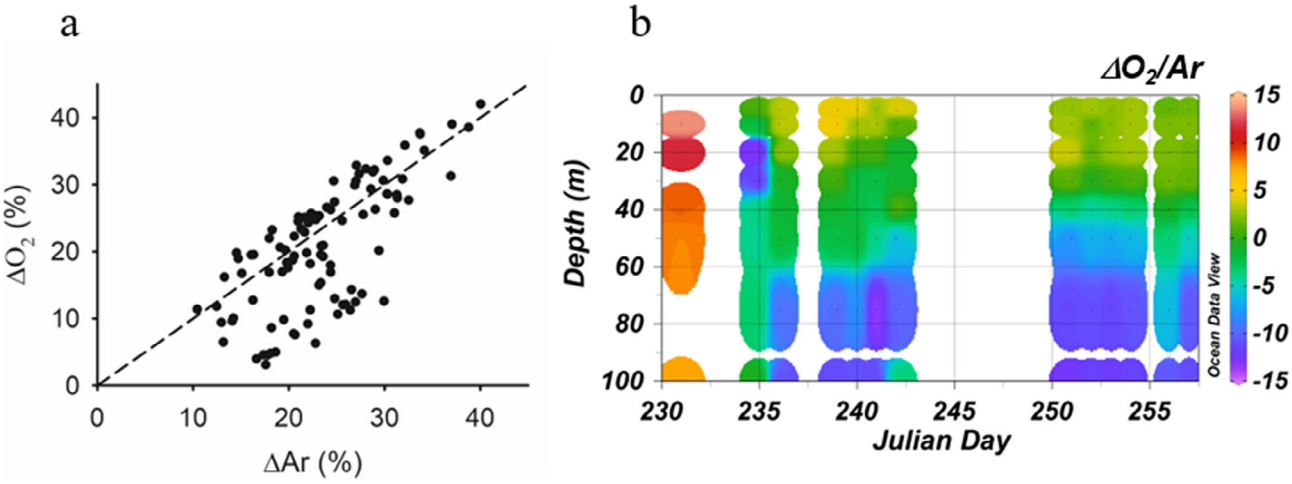

Fig 10. (**a**) Scatter plot of saturation anomalies of Ar vs. O_2 and (**b**) ΔO_2/Ar in the water column from days 231 to 257.

dicothermal layer (i.e., colder water sandwiched between warmer waters) started to erode due to brine exclusion during ice formation at the surface. This physical process has been frequently observed in surface Arctic waters (Pickard and Emery 1990).

Light and nutrient limiting conditions

The Central Arctic Ocean has previously been considered an ecosystem that is significantly light and nutrient limited (Li et al. 2009; Alou-Font et al. 2016; Stratmann et al. 2017). The current study supports these findings, specifically as late summer transitioned into early autumn. Even with the deepening of the mixed layer during the early autumn, entrainment of nutrient-enriched waters toward the surface was not observed, as the main nutricline remained at approximately 100 m (Fig. 5). Extensive nitrate limitation was observed in the surface waters throughout the entire sampling period, as nitrate concentrations were < 2 μmol L^{-1} (Fig. 5a) and N : P ratios were approximately 2–3, well below the Redfield ratio (Fig. 5e). Even though nitrate levels were very low in the upper 20 m, relatively high Fv/Fm values and positive $\Delta O_2/Ar$ values (indicators of phytoplankton photosynthetic competency and production, respectively) were observed, especially during the late summer when light transmittance values were highest (Figs. 4, 6, 10). We propose these high Fv/Fm and $\Delta O_2/Ar$ values were related to relatively high irradiance and ammonium levels. The fraction of total inorganic nitrogen available as regenerated nitrogen suggested that $\sim$ 50% of the nitrogenous nutrition was available as recycled ammonium, rather than nitrate during this time (Figs. 5, S4). This hypothesis is corroborated by the relatively high levels of phaeopigments observed, presumably from macrozooplankton grazing on microphytoplanktonic species seeded into the upper water column during sea ice melt conditions earlier in the summer (Figs. S4, S5). However, ^{15}N assimilation experiments would be needed to confirm the relative importance of recycled ammonium.

Phosphate was more depleted in the early autumn surface mixed layer, compared to late summer, as concentrations decreased from approximately 0.6 to 0.4 μmol L^{-1} (Fig. 5b). Although silicate concentrations were also low (2–6 μmol L^{-1}) in the surface waters, silicate-to-nitrate ratios suggested no significant silicate limitation effects with respect to nitrate (Fig. 5f). These low nitrate and phosphate concentrations at the surface most likely reflected seasonal nutrient drawdown. During the early autumn, phytoplankton TChl *a* biomass decreased daily, such that the lowest surface biomass was measured on day 257 (Fig. 6). This occurred in surface waters that became increasingly depleted of macronutrients, most likely due to phytoplankton uptake.

The resulting light and nutrient limiting conditions of early autumn (Figs. 4, 5) were correlated with lower TChl *a* biomass (Fig. 6a; Table 2), lower photosynthetic efficiency of PS II (as Fv/Fm, Fig. 6c), and lower $\Delta O_2/Ar$ ratios (Fig. 10) with respect to late summer values. These results suggest that our sampling period during the early autumn most likely marked the end of the high productivity season in the Central Arctic Ocean.

Phytoplankton community composition

We also hypothesized that a shift in the phytoplankton community toward picoeukaryotic cells would occur as nutrient and light co-limitation conditions progressed during the transition from late summer to early autumn. However, size-fractionated TChl *a* was dominated ($\sim$ 60%) by picoeukaryotes in both late summer and early autumn (Fig. 8). No significant changes in the community composition were detected either, as Chl c_3 flagellates and *Pyramimonas* spp. were the most prevalent groups observed throughout the entire sampling period (Fig. 7).

Despite a lack of temporal changes, the phytoplankton community of the Central Arctic Ocean was very diverse, as evidenced by the community evenness index (Table S5). Individuals from all nine algal groups identified in the CHEMTAX analysis were observed on all sampling days (Figs. 7, S6). Of the nine taxonomic groups, only the picoeukaryotic Chl c_3 flagellates and *Pyramimonas* spp. groups contributed close to 50% of the community at any given day or depth, and these two groups were consistently the most abundant algal groups present. *Pyramimonas* spp. represented 20% to 50% of TChl *a* biomass in surface waters (<10 m) where light levels were highest (Fig. 4), suggesting a strong light dependency. The Chl c_3 flagellate group allocated a similar percentage to TChl *a* in the lower photic zone (>10 m; Fig. S6). Prymnesiophytes, cryptophytes, chlorophytes, diatoms, and *Micromonas* spp. were the next most abundant groups, averaging approximately $\sim$10% of the community TChl *a* biomass, while dinoflagellates and chrysophytes-pelagophytes contributed less than 5% of the TChl *a* (Fig. 7).

Even though picophytoplankton were highly abundant in the surface waters throughout the late summer and early autumn periods, we observed that the composition of this community was more diverse than those noted in previous studies (e.g., Lovejoy et al. 2007; Li et al. 2009). Not only was this high biodiversity unexpected, but also intriguing was the fact that *Pyramimonas* spp. contributed a significantly higher percentage of the TChl *a* biomass than *Micromonas* spp., the Chl *b*-containing picoeukaryote previously seen dominating surface Arctic waters (Lovejoy et al. 2007; Li et al. 2009). The present study reported *Micromonas* spp. contributed only about 10% of the TChl *a*, while *Pyramimonas* spp., were more abundant (>25%), especially in the high light surface waters, and were significantly correlated with TChl *a* biomass (r = 0.448; Table S7). As the extent and duration of open, ice-free waters in the Central Arctic Ocean increases, light may become less limiting (depending on wind stress and convective mixing), potentially expanding the ecological niche of *Pyramimonas* spp.

Although CHEMTAX results can sometimes be biased by the initial pigment ratios chosen (Schlüter et al. 2000; Schlüter and Møhlenberg 2003), four lines of evidence support the CHEMTAX results obtained here, that revealed the relative dominance of *Pyramimonas* spp. compared to *Micromonas* spp. First, the fact that the final pigment ratio matrices from the CHEMTAX analysis were similar to the initial pigment ratio matrix used supports the relative accuracy of the results (Tables S3 and S4). Second, we compared the measured TChl *a* integrated values observed in the water column to those predicted by employing a separate multiple regression analysis of the major pigments measured (Fujiwara et al. 2014). The average TChl *a* concentration predicted from the multiple regression analysis of the accessory xanthophyll pigments was 82% ± 16% of the measured integrated TChl *a* values measured in the present study (Table 2). Third, the presence of Chl *b* and the lack of prasinoxanthin lends strong support to the CHEMTAX results, as *Micromonas* spp. contain prasinoxanthin and *Pyramimonas* spp. do not (Figs. S2, S3). Lastly, the average integrated water column ratio of prasinoxanthin : Chl *b* (~0.05; Table 2) was approximately fourfold lower than the ratio observed in a *Micromonas*-dominated community in the Western Arctic Ocean (Fujiwara et al. 2014).

While picoeukaryotes dominated the Central Arctic Ocean phytoplankton community in the present study, diatoms only contributed up to 10% of the TChl *a* biomass (Fig. 7). As diatoms often dominate the phytoplankton community in areas of high nutrients (e.g., Coupel et al. 2015), this may reflect the oligotrophic nature of the Central Arctic Ocean, especially in a highly stratified water column (Figs. 3, 5). In the Beaufort Sea, nitrate-rich surface waters along the shelf were dominated by diatoms, while oligotrophic, off-shore surface communities were characterized by high abundances of Chl *b*-containing algae, such as prasinoxanthin-containing prasinophytes (i.e., *Micromonas*; Coupel et al. 2015). Phytoplankton communities in both the Beaufort Sea and Baffin Bay contained greater proportions of diatoms when water column stratification was weaker (i.e., greater convective mixing) and shifted toward a flagellate (including prymnesiophytes) and picoeukaryote (mainly *Micromonas*)-dominated community as stratification increased (Blais et al. 2017). This increase in water column stratification was also suggested to have prevented the autumn diatom blooms that have become common throughout the Arctic in recent years (Ardyna et al. 2014; Blais et al. 2017). Other studies have shown similar picophytoplankton-dominated communities (Lovejoy et al. 2007), especially in areas of low nutrients (Li et al. 2009; Coupel et al. 2015) and high sea ice coverage (Gosselin et al. 1997), conditions that also characterized the environment in the present study, particularly during the early autumn.

Biogenic sulfur

The lack of measurable DMS concentrations in the water column did not result from a high detection limit, as previous studies have also found very low DMS concentrations in the Central Arctic Ocean. For instance, Leck and Persson (1996) reported values ranging from 2 nmol L^{-1} down to 0.02 nmol L^{-1} in the closed ice-pack zone of the Central Arctic Ocean with the lowest values being observed during freeze-up in mid-to-late September. Sharma et al. (1999) reported a surface water DMS concentration of 1.2 nmol L^{-1} at the North Pole in late August. More recently, during a similar ice-floe drift expedition, Matrai et al. (2008) observed subsurface DMS concentrations of 2 nmol L^{-1} at the beginning of August with concentrations falling to less than the limit of detection for their study by the end of August.

The DMSP values measured in the present study are directly comparable to the findings of Matrai et al. (2008) who reported $DMSP_d$ levels of 0–10 nmol L^{-1} and $DMSP_p$ levels of 0–30 nmol L^{-1}. Similarly, Damm et al. (2010) found $DMSP_t$ levels on the order of 0–30 nmol L^{-1} with a dramatic drop in $DMSP_t$ levels below a depth of 40 m in the Central Arctic Ocean. The modest levels of $DMSP_p$ and the low levels of DMS we observed may reflect either the lack of appreciable DMSP lyase activity or simply a net balance between DMS production and consumption.

Particulate DMSP concentrations were highly correlated with TChl *a* (r = 0.704) and pheophytin *a* (r = 0.552) concentrations (Fig. S7; Table S7). The correlation between $DMSP_p$ and these two variables can be explained by the consumption of phytoplankton via macrozooplankton grazing, as pheophytin *a* is a degradation product of Chl *a*. Qualitative evidence to support this hypothesis was collected by ROV dives that frequently observed abundant copepod populations and a bottom ice community visibly dominated by *Melosira* spp. (Fig. S5), a high DMSP-producing diatom (Keller et al. 1989). A positive correlation was also noted between $DMSP_p$ and *Pyramimonas* spp. (r = 0.509) and the Chl *b* : TChl *a* ratio (r = 0.434), while a weak, negative relationship was found with the Chl c_3 flagellates (r = −0.080; Table S7), the other dominant phytoplankton group. Since *Pyramimonas* spp. populations are frequently observed in Arctic sea ice communities (Harðardóttir et al. 2014), it is conceivable that the positive correlation between $DMSP_p$ and *Pyramimonas* spp. observed in our study may be related to $DMSP_p$ serving an osmoprotective or cryoprotective function in this species. Similar to *Phaeocystis* spp., it is likely that there exists significant interspecific and intraspecific variability in $DMSP_p$ levels for polar *Pyramimonas* spp. For example, an Antarctic species of *Pyramimonas* spp. had similar DMSP production rates as *P. antarctica* (Sheehan and Petrou 2020). Clearly, more research is warranted on the role of *Pyramimonas* spp. on the biogeochemical sulfur cycle of the Arctic Ocean.

ΔO_2/Ar ratios

A comparison of the ΔO_2/Ar results obtained during this study with results from other global locations is given in Table S6. Estimates of ΔO_2/Ar ratios for the Central Arctic Ocean region have been reported to be approximately 0–4 near the North Pole (Eveleth et al. 2014; Ulfsbo et al. 2014). Those findings point to the Arctic Ocean being more comparable to open-ocean oligotrophic regions (e.g., Emerson et al. 1991; Juranek et al. 2012) rather than more productive polar coastal seas (e.g., Tortell et al. 2011, 2012; Eveleth et al. 2017). Given the very low levels of phytoplankton biomass observed during this study, it is likely that seasonal oxygen accumulation from photosynthesis is greater than community respiration and is driving the observed near-surface oxygen supersaturation during the late summer period.

The impact of ice cover on oxygen saturation has long been understood (reviewed by Eveleth et al. 2014). Melting of sea ice increases O_2 saturation while sea-ice formation decreases it. Moreover, the presence of sea ice provides a physical barrier that restricts atmospheric exchange and prevents bubble injection from breaking waves thereby increasing the residence time for oxygen. Thus, the positive ΔO_2/Ar anomalies observed in the relatively quiescent near-surface water column around and below the ice floe very likely resulted from these processes. The presence of positive ΔAr anomalies (Fig. 10) also supports the idea that freezing processes and poor atmospheric exchange are important in this environment (Eveleth et al. 2014). Below the mixed layer depth, the observed undersaturation likely resulted from microbial respiration processes.

Conclusions

In this study, we measured a large suite of physical, biogeochemical, and ecological parameters along a drifting ice floe in the Central Arctic Ocean, close to the North Pole ($\sim$ 89.5°N). Our expedition was conducted from late summer (19 August 2018) to the start of refreezing in early autumn (14 September 2018), a period when few observations have been recorded in this region. Significant changes in hydrography and nutrient and light availability were observed during this critical seasonal transition, while phytoplankton community structure remained fairly constant. These observations revealed that near surface waters of the Central Arctic Ocean in late summer remain a light and nutrient-limited, oligotrophic-like environment with a diverse picoautotrophic community lacking a single major (>50%) taxonomic group. Within the surface mixed layer, the Chl c_3-containing flagellate group and *Pyramimonas* spp. dominated the TChl *a* biomass in this region, not the typically observed *Micromonas* spp. Measured concentrations of $DMSP_p$ were relatively low but, surprisingly, positively correlated with *Pyramimonas* spp., a Chl *b*-containing prasinophyte not usually considered a high DMSP producer.

In the near future, significant wind stress across an ice-free Arctic Ocean will likely erode water column stratification in the late summer and thereby affect turbulent diffusive nutrient fluxes across the halocline. However, even with the loss of sea ice cover in late summer, oligotrophic conditions may still persist in this region given a nutricline depth of $\sim$ 100 m and the kinetic energy required for nutrient fluxes to reach the photic zone. In addition, as climate change will lead to the complete loss of summer sea ice cover, enhanced irradiance levels within the surface mixed layer will likely relieve light limitation effects in the late summer and lead to enhanced net community production (i.e., positive ΔO_2/Ar values). Yet, it is also possible that significant wind stress could lead to enhanced vertical mixing and lower the average irradiance experienced by phytoplankton. The results of the present study suggest that picoprasinophytes, such as *Pyramimonas* spp., may become a more dominant component of the phytoplankton community of the future Central Arctic Ocean, as this group was observed to be highly light dependent and abundant in a nutrient-deplete water column. Potential nutrient fluxes into the photic zone will likely set the maximum biomass possible and light-nutrient interactions will determine the community composition within the Central Arctic Ocean. These changes will significantly impact DMSP production and the fluxes of climatically active gases, such as DMS, into the atmosphere. As summer sea ice rapidly thins in the Central Arctic Ocean continued observations of productivity, phytoplankton community dynamics and biogeochemical cycling will be paramount to understanding climate change impacts on this temporally evolving ecosystem.

References

Alou-Font, E., S. Roy, S. Agustí, and M. Gosselin. 2016. Cell viability, pigments and photosynthetic performance of Arctic phytoplankton in contrasting ice-covered and open-water conditions during the spring–summer transition. Mar. Ecol. Prog. Ser. **543**: 89–106. doi:10.3354/meps11562

Ardyna, M., M. Babin, M. Gosselin, E. Devred, L. Rainville, and J. Tremblay. 2014. Recent Arctic Ocean sea ice loss triggers novel fall phytoplankton blooms. Geophys. Res. Lett. **41**: 6207–6212. doi:10.1002/2014GL061047

Arrigo, K. R., G. L. van Dijken, and S. Pabi. 2008. Impact of shrinking Arctic ice cover on marine primary production. Geophys. Res. Lett. **35**: L19603. doi:10.1029/2008GL035028

Barak-Gavish, N., et al. 2018. Bacterial virulence against an oceanic bloom-forming phytoplankter is mediated by algal DMSP. Sci. Adv. **4**: eaau5716. doi:10.1126/sciadv.aau5716

Blais, M., M. Ardyna, M. Gosselin, D. Dumont, S. Bélanger, J. Tremblay, Y. Gratton, C. Marchese, and M. Poulin. 2017. Contrasting interannual changes in phytoplankton productivity and community structure in the coastal Canadian Arctic Ocean. Limnol. Oceanogr. **62**: 2480–2497. doi:10.1002/lno.10581

Carmack, E., and P. Wassmann. 2006. Food webs and physical–biological coupling on pan-Arctic shelves: Unifying concepts and comprehensive perspectives. Prog. Oceanogr. **71**: 446–477. doi:10.1016/j.pocean.2006.10.004

Charlson, R. J., J. E. Lovelock, M. O. Andreae, and S. G. Warren. 1987. Oceanic phytoplankton, atmospheric sulphur, cloud albedo and climate. Nature **326**: 655–661.

Codispoti, L. A., C. Flagg, V. Kelly, and J. H. Swift. 2005. Hydrographic conditions during the 2002 SBI process experiments. Deep-Sea Res. II Top. Stud. Oceanogr. **52**: 3199–3226. doi:10.1016/j.dsr2.2005.10.007

Codispoti, L. A., V. Kelly, A. Thessen, P. Matrai, S. Suttles, V. Hill, M. Steele, and B. Light. 2013. Synthesis of primary production in the Arctic Ocean III: Nitrate and phosphate-based estimates of net community production. Prog. Oceanogr. **110**: 126–150. doi:10.1016/j.pocean.2012.11.006

Coupel, P., A. Matsuoka, D. Ruiz-Pino, M. Gosselin, D. Marie, J.-É. Tremblay, and M. Babin. 2015. Pigment signatures of phytoplankton communities in the Beaufort Sea. Biogeosciences **12**: 991–1006. doi:10.5194/bgd-11-14489-2014

Cullen, J. J., and R. F. Davis. 2003. The blank can make a big difference in oceanographic measurements. Limnol. Oceanogr. Bull. **12**: 29–35.

Damm, E., E. Helmke, S. Thoms, U. Schauer, E. Nöthig, K. Bakker, and R. P. Kiene. 2010. Methane production in aerobic oligotrophic surface water in the Central Arctic Ocean. Biogeosciences **7**: 1099–1108.

Damm, E., B. Rudels, U. Schauer, S. Mau, and G. Dieckmann. 2015. Methane excess in Arctic surface water-triggered by sea ice formation and melting. Sci. Rep. **10**: 16179. doi:10.1038/srep16179

Demory, D., and others. 2019. Picoeukaryotes of the micromonas genus: Sentinels of a warming ocean. ISME J. **13**: 132–146. doi:10.1038/s41396-018-0248-0

DiTullio, G. R., D. L. Garrison, and S. Mathot. 1998. Dimethylsulfoniopropionate in sea ice algae from the Ross Sea polynya. Antarctic Res. Ser. **73**: 139–146.

DiTullio, G. R., and M. E. Geesey. 2002. Photosynthetic pigments in marine algae and bacteria, p. 2453–2470. *In* G. Bitton [eds.], The encyclopedia of environmental microbiology. John Wiley & Sons. New York. doi:10.1002/0471263397.env185

DiTullio, G. R., M. E. Geesey, D. R. Jones, K. L. Daly, L. Campbell, and W. O. Smith Jr. 2003. Phytoplankton assemblage structure and primary productivity along 170° W in the South Pacific Ocean. Mar. Ecol. Prog. Ser. **255**: 55–80.

Emerson, S., P. Quay, C. Stump, D. Wilbur, and M. Knox. 1991. O_2, Ar, N_2, and ^{222}Rn in surface waters of the subarctic ocean: Net biological O_2 production. Global Biogeochem. Cycles **5**: 49–69.

Eppley, R. W., and B. J. Peterson. 1979. Particulate organic matter flux and planktonic new production in the deep ocean. Nature **282**: 677–680.

Eveleth, R., M. L. Timmermans, and N. Cassar. 2014. Physical and biological controls on oxygen saturation variability in the Upper Arctic Ocean. J. Geophy. Res. Oceans **119**: 7420–7432. doi:10.1002/2014JC009816

Eveleth, R., N. Cassar, R. M. Sherrell, H. Ducklow, M. P. Meredith, H. J. Venables, Y. Lin, and Z. Li. 2017. Ice melt influence on summertime net community production along the Western Antarctic Peninsula. Deep-Sea Res. II Top. Stud. Oceanogr. **139**: 89–102. doi:10.1016/j.dsr2.2016.07.016

Fujiwara, A., T. Hirawake, K. Suzuki, I. Imai, and S. I. Saitoh. 2014. Timing of sea ice retreat can alter phytoplankton community structure in the Western Arctic Ocean. Biogeosciences **11**: 1705–1716.

Genty, B., J.-M. Briantais, and N. R. Baker. 1989. The relationship between the quantum yield of photosynthetic electron transport and quenching of chlorophyll fluorescence. Biochim. Biophys. Acta **990**: 87–92.

Gosselin, M., M. Levasseur, P. A. Wheeler, R. A. Horner, and B. C. Booth. 1997. New measurements of phytoplankton and ice algal production in the Arctic Ocean. Deep-Sea Res. II Top. Stud. Oceanogr. **44**: 1623–1644.

Gradinger, R. 1996. Occurrence of an algal bloom under Arctic pack ice. Mar. Ecol. Prog. Ser. **131**: 301–305.

Hamme, R. C., N. Cassar, V. P. Lance, R. D. Vaillancourt, M. L. Bender, P. G. Strutton, T. S. Moore, M. D. DeGrandpre, C. L. Sabine, and D. T. Ho. 2012. Dissolved O2/Ar and other methods reveal rapid changes in productivity during a Lagrangian experiment in the Southern Ocean. Journal of Geophysical Research: Oceans **117**: (C4). doi:10.1029/2011jc007046

Harðardóttir, S., N. Lundholm, Ø. Moestrup, and T. G. Nielsen. 2014. Description of *Pyramimonas diskoicola* sp. nov. and the importance of the flagellate Pyramimonas (Prasinophyceae) in Greenland Sea ice during the winter–spring transition. Polar Biol. **37**: 1479–1494.

Harrison, P. J., R. E. Waters, and F. R. J. Taylor. 1980. A broad spectrum seawater medium for coastal and open ocean phytoplankton. J. Phycol. **16**: 28–35.

Holm-Hansen, O., C. J. Lorenzen, R. W. Holmes, and J. D. H. Strickland. 1965. Fluorometric determination of chlorophyll. ICES J. Mar. Sci. **30**: 3–15.

Holland, M. M., and C. M. Bitz. 2003. Polar amplification of climate change in coupled models. Climate Dynam. **21**: 221–232.

Hoppe, C. J. M., C. M. Flintrop, and B. Rost [eds.]. 2018. The Arctic picoeukaryote *Micromonas pusilla* benefits synergistically from warming and ocean acidification. Biogeosciences **15**: 4353–4365. doi:10.5194/bg-15-4353-2018

Juranek, L. W., P. D. Quay, R. A. Feely, D. Lockwood, D. M. Karl, and M. J. Church. 2012. Biological production in the NE Pacific and its influence on air-sea CO_2 flux: Evidence from dissolved oxygen isotopes and O_2/Ar. J. Geophys. Res. Oceans. **117**: C05022. doi:10.1029/2011JC007450

Katlein, C., M. Schiller, H. J. Belter, V. Coppolaro, D. Wenslandt, and M. Nicolaus. 2017. A new remotely operated sensor platform for interdisciplinary observations under sea ice. Front. Mar. Sci. **4**. doi:10.3389/fmars.2017.00281

Keller, M. D., W. K. Bellows, and R. R. Guillard. 1989. Dimethyl sulfide production in marine phytoplankton, p. 167–182. *In* E. S. Saltzman and W. J. Cooper [eds.], Biogenic sulfur in the environment. American Chemical Society.

Kiene, R. P., and D. Slezak. 2006. Low dissolved DMSP concentrations in seawater revealed by small-volume gravity filtration and dialysis sampling. Limnol. Oceanogr.: Methods. **4**: 80–95.

Kinsey, J. D., and D. J. Kieber. 2016. Microwave preservation method for DMSP, DMSO, and acrylate in unfiltered seawater and phytoplankton culture samples. Limnol. Oceanogr. Methods **14**: 196–209. doi:10.1002/lom3.10081

Knauss, J. A., and N. Garfield. 2017. Introduction to physical oceanography, 3rd ed. Long Grove, IL: Waveland PressInc.

Leck, C., and C. Persson. 1996. The Central Arctic Ocean as a source of dimethyl sulfide seasonal variability in relation to biological activity. Tellus B **48**: 156–177. doi:10.3402/tellusb.v48i2.15834

Lee, Y., J. Min, E. J. Yang, K. Cho, J. Jung, J. Park, J. K. Moon, and S. Kang. 2019. Influence of sea ice concentration on phytoplankton community structure in the Chukchi and East Siberian Seas, Pacific Arctic Ocean. Deep Sea Res. Part I **147**: 54–64. doi:10.1016/j.dsr/2019.04/001

Levasseur, M., M. Gosselin, and S. Michaud. 1994. A new source of dimethylsulfide (DMS) for the arctic atmosphere: Ice diatoms. Mar. Biol. **121**: 381–387.

Levitus, S. 1982. Climatological atlas of the world ocean. NOAA Professional Paper 13. U.S. Govt. Print. Off.

Lewis, K. M., and others. 2019. Photoacclimation of Arctic Ocean phytoplankton to shifting light and nutrient limitation. Limnol. Oceanogr. **64**: 284–301. doi:10.1002/lno.11039

Li, W. K. W., F. A. McLaughlin, C. Lovejoy, and E. C. Carmack. 2009. Smallest algae thrive as the Arctic Ocean freshens. Science **326**: 539. doi:10.1126/science.1179798

Lovejoy, C., W. F. Vincent, S. Bonilla, S. Roy, M.-J. Martineau, R. Terrado, M. Potvin, R. Massana, and C. Pedrós-Alió. 2007. Distribution, phylogeny, and growth of cold-adapted picoprasinophytes in Arctic seas. J. Phycol. **43**: 78–89. doi:10.1111/j.1529-8817/2006/00310.x

Lyon, B. R., J. M. Bennett, P. A. Lee, M. Janech, and G. R. DiTullio. 2016. Role of dimethyl-sulfoniopropionate as an osmoprotectant following gradual salinity shifts in the sea-ice diatom *Fragilariopsis cylindrus*. Environ. Chem. **13**: 181–194. doi:10.1071/EN14269

Mackey, M. D., D. J. Mackey, H. W. Higgins, and S. W. Wright. 1996. CHEMTAX-a program for estimating class abundances from chemical markers: Application to HPLC measurements of phytoplankton. Mar. Ecol. Prog. Ser. **144**: 265–283.

Matrai, P. A., L. Tranvik, C. Leck, and J. C. Knulst. 2008. Are high Arctic surface microlayers a potential source of aerosol organic precursors? Mar. Chem. **108**: 109–122. doi:10.1016/j.marchem.2007.11.001

Maxwell, K., and G. N. Johnson. 2000. Chlorophyll fluorescence—a practical guide. J. Exp. Bot. **51**: 659–668. doi:10.1093/jxb.51.345.659

Meredith, M., and others. 2019. Polar Regions. *In* H.-O. Pörtner et al. [eds.], IPCC special report on the ocean and cryosphere in a changing climate. In press. Cambridge University Press.

Nicholson, D., S. Emerson, N. Caillon, J. Jouzel, and R. C. Hamme. 2010. Constraining ventilation during Deepwater formation using deep ocean measurements of the dissolved gas ratios 40Ar/36Ar, N2/Ar, and Kr/Ar. J. Geophys. Res. Oceans **115**: C11015. doi:10.1029/2010JC006152

Nicolaus, M., and C. Katlein. 2013. Mapping radiation transfer through sea ice using a remotely operated vehicle (ROV). Cryosphere **7**: 763–777.

Overland, J. E., and M. Wang. 2013. When will the summer Arctic be nearly ice free? Geophys. Res. Lett. **40**: 2097–2101.

Pickard, G. L., and W. J. Emery. 1990. Descriptive physical oceanography, 5th ed. Oxford, UK: Pergamon Press.

Popova, E. E., A. Yool, A. C. Coward, Y. K. Aksenov, S. G. Alderson, B. A. de Cuevas, and T. R. Anderson. 2010. Control of primary production in the Arctic by nutrients and light: Insights from a high-resolution ocean general circulation model. Biogeosciences **7**: 3569–3591. doi:10.5194/bgd-7-557-2010

Prytherch, J. 2019. Micrometeorological data from icebreaker Oden's foremast during the Arctic Ocean 2018 expedition. Bolin Center Database. Version 2.0. Bolin Centre Database. https://bolin.su.se/data/ao2018-micromet-oden

Schlüter, L., F. Møhlenberg, H. Havskum, and S. Larsen. 2000. The use of phytoplankton pigments for identifying and quantifying phytoplankton groups in coastal areas: Testing the influence of light and nutrients on pigment/chlorophyll a ratios. Mar. Ecol. Prog. Ser. **192**: 49–63.

Schlüter, L., and F. Møhlenberg. 2003. Detecting presence of phytoplankton groups with non-specific pigment signatures. J. Appl. Phycol. **15**: 465–476.

Sharma, S., L. A. Barrie, D. Plummer, J. C. McConnell, P. C. Brickell, M. Levasseur, M. Gosselin, and T. S. Bates. 1999. Flux estimation of oceanic dimethyl sulfide around North America. J. Geophys. Res. Atmos. **104**: 21327–21342.

Sheehan, C. E., and K. Petrou. 2020. Dimethylated sulfur production in batch cultures of Southern Ocean phytoplankton. Biogeochemistry **147**: 53–69.

Sherr, E. B., and B. F. Sherr. 2002. Significance of predation by protists in aquatic microbial food webs. Antonie Van Leeuwenhoek **81**: 293–308.

Stefels, J. 2000. Physicological aspects of the production and conversion of DMSP in marine algae and higher plants. J. Sea Res. **43**: 183–197.

Stratmann, T., L. C. Lund-Hansen, B. K. Sorrell, and S. Markager. 2017. Concentrations of organic and inorganic bound nutrient and chlorophyll a in the Eurasian Basin, Arctic Ocean, early autumn 2012. Reg. Stud. Mar. Sci. **9**: 69–75. doi:10.1016/j.rsma.2016.11.008

Tortell, P. D., C. Guéguen, M. C. Long, C. D. Payne, P. Lee, and G. R. DiTullio. 2011. Spatial variability and temporal dynamics of surface water pCO_2, $\Delta O_2/Ar$ and dimethylsulfide in the Ross Sea, Antarctica. Deep-Sea Res. I Oceanogr. Res. Pap. **58**: 241–259. doi:10.1016/j.dsr.2010.12.006

Tortell, P. D., M. C. Long, C. D. Payne, C. A. Alderkamp, P. Dutrieux, and K. R. Arrigo. 2012. Spatial distribution of pCO_2, $\Delta O_2/Ar$ and dimethylsulfide (DMS) in polynya waters and the sea ice zone of the Amundsen Sea, Antarctica. Deep-Sea Res. II Top. Stud. Oceanogr. **71**: 77–93. doi:10.1016/j.dsr2.2012.03.010

Tortell, P. D., et al. 2014. Metabolic balance of coastal Antarctic waters revealed by autonomous pCO_2 and $\Delta O_2/Ar$ measurements. Geophys. Res. Lett. **16**: 6803–6810. doi:10.1002/2014GL061266

Tremblay, J., and J. Gagnon. 2009. The effects of irradiance and nutrient supply on the productivity of Arctic waters: A perspective on climate change, p. 73–89. *In* J. C. J. Nihoul and A. G. Kostianoy [eds.], Influence of climate change on the changing Arctic and sub-Arctic conditions. Springer.

Ulfsbo, A., N. Cassar, M. Korhonen, S. van Heuven, M. Hoppema, G. Kattner, and L. G. Anderson. 2014. Late summer net community production in the Central Arctic Ocean using multiple approaches. Global Biogeochem. Cycles **28**: 1129–1148. doi:10.1002/2014GB004833

Worden, A. Z., and others. 2009. Green evolution and dynamic adaptations revealed by genomes of the marine picoeukaryotes *Micromonas*. Science **324**: 268–272.

Worden, A. Z., M. J. Follows, S. J. Giovannoni, S. Wilken, A. E. Zimmerman, and P. J. Keeling. 2015. Rethinking the marine carbon cycle: Factoring in the multifarious lifestyles of microbes. Science **347**: 1257594. doi:10.1126/science/1257594

Yamamoto, S., J. B. Alcauskas, and T. E. Crozier. 1976. Solubility of methane in distilled water and seawater. J. Chem. Eng. Data **21**: 78–80.

Acknowledgments

The authors are indebted to the Captain and crew of the RVIB *Oden* and the staff of the Swedish Polar Research Secretariat, without whose support this project would not have been possible. The authors would also like to thank Chief Scientists Caroline Leck and Patricia Matrai for their organization of the expedition. A special thanks to Walker Smith for the use of the Phyto PAM phytoplankton analyzer and to James Cumming for his assistance in collecting and processing samples during the expedition. This work has been made possible by support from the U.S. National Science Foundation through grants PLR-1736783 (Arctic Natural Sciences) to G.R.D. and P.A.L. and OCE-1436458 (Biological Oceanography) to P.A.L. and G.R.D. ROV operations were funded by the Helmholtz infrastructure initiative "FRAM" (Frontiers in Arctic marine Monitoring) and supported by the Diatom ARCTIC project (NE/R012849/1; 03F0810A), part of the Changing Arctic Ocean program, jointly funded by the UKRI Natural Environmental Research Council (NERC) and the German Federal Ministry of Education and Research (BMBF). This article is contribution number 547 to the Graduate Program in Marine Biology at the College of Charleston, Charleston, South Carolina.

Conflict of Interest

The authors declare no conflict of interest. The funding sponsors had no role in the design of the study, in the collection, analyses, or interpretation of data, in the writing of the manuscript, or in the decision to publish the results. Any opinions, findings, and conclusions or recommendations expressed in this material are those of the author(s) and do not necessarily reflect the views of the National Science Foundation or the Swedish Polar Research Secretariat. Furthermore, commercial equipment or materials are identified in this paper to specify adequately the experimental procedure. Such identification does not imply recommendation or endorsement by the National Science Foundation or the Swedish Polar Research Secretariat, nor does it imply that the materials or equipment identified are necessarily the best available for the purpose.

Submitted 31 January 2020
Revised 24 July 2020
Accepted 23 November 2020

Associate editor: Ronnie N. Glud